

1 **Estimating Ground Motion Intensities Using Simulation-Based Estimates of Local**
2 **Crustal Seismic Response**

3 **Himanshu Agrawal¹ and John McCloskey^{1†}**

4 ¹School of Geosciences, University of Edinburgh, Drummond Street Edinburgh, Edinburgh EH8
5 9XP, UK

6 [†]Deceased

7 Corresponding author: Himanshu Agrawal (himanshu.agrawal@ed.ac.uk),
8 (himansh78@gmail.com)

9 **Key Points:**

- 10 • In the Global South, the absence of seismic catalogues impedes ground motion
11 predictions that are crucial for earthquake-aware urban planning.
- 12 • Physics-based simulations can use hypothetical earthquakes to estimate ground motions
13 without extensive earthquake data availability.
- 14 • The primary source of short-scale variability in ground motion is the local subsurface
15 geology, making it a crucial focal point.

16 **Abstract**

17 It is estimated that 2 billion people will move to cities in the next 30 years, many of which
18 possess high seismic risk, underscoring the importance of reliable hazard assessments. Current
19 ground motion models for these assessments typically rely on an extensive catalogue of events to
20 derive empirical Ground Motion Prediction Equations (GMPEs), which are often unavailable in
21 developing countries. Considering the challenge, we choose an alternative method utilizing
22 physics-based (PB) ground motion simulations, and develop a simplified decomposition of
23 ground motion estimation by considering regional attenuation (Δ) and local site amplification
24 (A), thereby exploring how much of the observed variability can be explained solely by wave
25 propagation effects. We deterministically evaluate these parameters in a virtual city named
26 Tomorrowville, located in a 3D layered crustal velocity model containing sedimentary basins,
27 using randomly oriented extended sources. Using these physics-based empirical parameters (Δ
28 and A), we evaluate the intensities, particularly Peak Ground Accelerations (PGA), of
29 hypothetical future earthquakes. The results suggest that the estimation of PGA using the
30 deterministic $\Delta - A$ decomposition exhibits a robust spatial correlation with the PGA obtained
31 from simulations within Tomorrowville. This method exposes an order of magnitude spatial
32 variability in PGA within Tomorrowville, primarily associated with the near surface geology and
33 largely independent of the seismic source. In conclusion, advances in PB simulations and
34 improved crustal structure determination offer the potential to overcome the limitations of
35 earthquake data availability to some extent, enabling prompt evaluation of ground motion
36 intensities.

37

38 **Plain Language Summary**

39 Numerous cities in earthquake-prone regions of the Global South are currently experiencing
40 rapid growth, which poses a significant risk to their populations in the upcoming years. The
41 attainment of effective urban planning, which takes earthquake vulnerabilities into account,
42 typically needs access to long-term earthquake recordings for projecting ground shaking through
43 to future seismic events. Regrettably, the scarcity of earthquake monitoring disproportionately
44 hampers this potential in the Global South, resulting in the utilization of ground motion data
45 from distant locations across the globe. This approach, however, comes with notable limitations

46 and contributes to the large uncertainty surrounding predictions of ground shaking. We approach
47 this challenge by employing state-of-the-art physics-based simulation techniques that can use
48 hypothetical earthquakes and numerically solve the seismic wave propagation through the
49 Earth's crust. Our study shows that even when a comprehensive earthquake database is lacking,
50 it is feasible to generate reasonably accurate predictions of the spatial variability in expected
51 ground motions using high-resolution local geological information. We emphasize that in cases
52 where urban planning choices need to be formulated for a city characterized by diverse
53 geological features, substantial investments in the measurement of subsurface properties can
54 prove valuable.

55

56 **1 Introduction**

57 The United Nations Human Settlements Programme (UN-Habitat) forecasts that by 2050 some 2
58 billion new citizens will move to urban centers so that, by then, some 68% of the world's
59 population will live in cities (UN-Habitat, 2022). It is estimated that 95% of this urbanization
60 will happen in the global south. Urban population growth is often accommodated by rapid urban
61 expansion in areas with well-documented seismic risk. The problems of understanding and
62 reducing disaster risk in such rapid development are significant, and while this expansion
63 presents a major global challenge, it also provides a time-limited opportunity to provide
64 evidence-based decision support for this new development (UNISDR, 2015). Efforts in
65 earthquake risk reduction through urban planning guided by high-resolution hazard assessment,
66 could reduce disaster risk for hundreds of millions of these future citizens. This approach also
67 provides a cost-efficient method by concentrating on new constructions, where the expenses
68 related to implementing effective earthquake-resistant design and construction are significantly
69 lower compared to the costs of retrofitting at a later stage.

70 Seismic hazard analysis informs building codes constraining construction of new development in
71 earthquake prone areas through development of ground motion models (Baker et al., 2021;
72 Bradley, 2019; Kramer, 1996; Kramer & Mitchell, 2006; Mcguire, 2008; Stirling, 2014; Stirling
73 et al., 2012). Observed ground shaking is a result of the interaction between a range of
74 individually heterogeneous fields and processes, leading to deep complexity in even the simplest

75 relationships. Measures of ground shaking intensity, for example, show an expected systematic
76 decrease with distance between the observation and source, but the systematics are overprinted
77 by the interactions between the complexities of the event and the crustal volume explored by the
78 seismic wave train. The result is high amplitude variability in the observed intensity. Note that
79 the uncertainty in the observations, in either intensity or distance, makes only a small
80 contribution to this variability; the variability is an intrinsic part of the process.

81 Consider a series of events recorded at large number of sensors. In the commonly applied
82 approach, the analyst chooses a functional form for the systematic decay of intensity and uses
83 some fitting procedure to estimate its parameters. The resulting model is commonly known as a
84 Ground Motion Model (GMM) (Douglas & Aochi, 2008; Douglas & Edwards, 2016a, 2016b),
85 and takes the form:

$$86 \quad \ln IM = \mu_{\ln IM} + \sigma_{\ln IM} \cdot \epsilon \quad (1)$$

87 Where, IM is the required intensity measure, $\mu_{\ln IM}$, is the estimated mean-field intensity, $\sigma_{\ln IM}$,
88 is an estimate of the variability around the mean which is usually assumed to conform to a log-
89 normal distribution and ϵ is the standard normal variate.

90 It is important to note that the $\mu_{\ln IM}$ term does not just describe the attenuation of intensity with
91 distance. Common forms of $\mu_{\ln IM}$ attempt to parameterize descriptions of the physics of the
92 entire process including source properties, such as focal mechanism and their resulting
93 directivity, as well as the local response of the site using estimates of V_{s30} (time-averaged shear-
94 wave velocity in the top 30m) and κ (high frequency attenuation parameter) for example (Aki,
95 1993; Borchardt & Glassmoyer, 1992; Bradley, 2011; Hough & Anderson, 1988; Kaklamanos et
96 al., 2013; Shi & Asimaki, 2017). Expressions for $\mu_{\ln IM}$ in current GMMs include numerous
97 parameters, use advanced statistical techniques to fit these complex functions, and represent a
98 practical approach to a fundamentally intractable problem (Douglas & Edwards, 2016a).

99 In practice, an ergodic assumption is invoked in GMM development by aggregating the data
100 from multiple spatial locations that is assumed to be equivalent to the distribution in time
101 (Anderson & Brune, 1999). However, with the increasing data for a particular tectonic area, the
102 non-ergodic or partial non-ergodic approaches are favoured which modify $\mu_{\ln IM}$ and $\sigma_{\ln IM}$ based
103 on calibration with the local data that is available (Bradley, 2015; Rodriguez-Marek et al., 2014;
104 Stewart et al., 2017). It is observed that major component of ground motion amplification can be

105 associated with the local geological factors e.g. sedimentary basins (Graves et al., 1998; Pilz et
106 al., 2011; Zhu et al., 2018), surface topography (Lee et al., 2009; Maufroy et al., 2012; G. Wang
107 et al., 2018), and soil conditions (Bazzurro & Cornell, 2004; Cramer, 2003; Torre et al., 2020).
108 Hence, the general practice in GMM development is dominated by using near-surface site-
109 specific parameters (for example V_{s30} and κ). It is suggested that these near-surface parameters
110 might exhibit strong correlations with geological features at greater depths, like basin depth
111 parameters (Z_{xx}) (Chiou & Youngs, 2014; Kamai et al., 2016; Tsai et al., 2021), and
112 consequently the amplification. However, opposing studies show that the amplification patterns
113 might not necessarily correlate with these parameters (Castellaro et al., 2008; Mucciarelli &
114 Gallipoli, 2006; Pitalakis et al., 2019), for example, sites with velocity profiles which are not
115 monotonically increasing with depth. This highlights the necessity to investigate more regional
116 geological structure to better understand the complexities of ground motion amplification.

117 Recently, the advances in computational capabilities and understanding the physical processes
118 have made it possible to use physics-based (PB) simulations for modelling ground motions
119 (Bradley, 2019; Graves & Pitarka, 2010; Smerzini & Villani, 2012; Taborda et al., 2014). PB
120 simulations are carried out by numerical modelling of the entire process of rupture
121 characterization and seismic wave propagation through the potentially complex Earth's crust.
122 However, the high computational cost and complex input requirements associated with them
123 restrict the large-scale usage of these methods, particularly in 3D. As a consequence the relative
124 contribution of these processes to the total observed variability has been relatively unexplored
125 compared to that of local shallow (decametre) site conditions.

126 Two immediate problems emerge in enacting the current ground motion modelling approaches in
127 the context of rapid urbanization in Global South, described above. Firstly, understanding ground
128 motion requires extensive seismic databases recording appropriate measures of intensity from a
129 large number of earthquakes, recorded at a network of sensors in the area of interest, for
130 example, PEER-NGA databases (Ancheta et al., 2014; Atkinson & Boore, 2006; Spudich et al.,
131 2013). Such catalogues necessitate the deployment of seismometers for many years even in the
132 most seismically active areas that is not possible to address the current time-critical problem
133 (Freddi et al., 2021). Secondly, urban development projects require hazard information at
134 unusually high resolution. Urban flood modelling and landslide susceptibility estimates, for
135 example, typically strive to use digital terrain models with 2-meter resolution supplemented by

136 high-resolution geotechnical assessments (Jenkins et al., 2023). Seismic intensity also varies
137 significantly over the scale of interest for urban planning, particularly where development is
138 planned over sedimentary basins or near to coasts or rivers with strong spatial contrasts in sub-
139 surface seismic velocity (Bielak et al., 1999; see also, Cadet et al., 2011; Foti et al., 2019). Some
140 efforts have been made to incorporate these factors into GMPEs (Abrahamson et al., 2014;
141 Campbell & Bozorgnia, 2014; Chiou & Youngs, 2014; Marafi et al., 2017), however, the
142 extensive information required to accurately characterize such effects remains a challenge. As a
143 result, the potential for high cost-benefit risk reduction that would accrue from high-resolution
144 understanding of ground motion variability remains elusive. Typically, GMMs developed in
145 data-rich countries of the global north are reconditioned for deployment in areas for which they
146 have no obvious physical validity (Hough et al., 2016; Nath & Thingbaijam, 2011). At best, this
147 leads to poor spatial resolution precluding the detailed site classification that is critical for
148 seismic microzonation studies needed for cost-effective urban planning (Ansal et al., 2010). The
149 development of appropriate techniques for rapid, local, high-resolution seismic hazard
150 assessment is a significant global challenge.

151 In this research, we approach this challenge by using a simplified decomposition of ground
152 motions into parametric relations explaining the regional and local variations in the measured
153 intensity. We focus on the effects only due to the sedimentary basins, which are known to
154 enhance the amplitude and duration of seismic waves through frequency-dependent focusing,
155 trapping and resonance (Castellaro & Musinu, 2023; Frankel, 1993; Yomogida & Etgen, 1993).
156 We demonstrate the usefulness of PB simulations in capturing the primary low frequency (LF),
157 $<1\text{Hz}$, sedimentary basin effects that contribute to the variation in ground motion within an
158 *urban* area situated within a seismically active region. We show, to first order, seismic intensity
159 decays along the wave path according to the integrated rheological properties of the region and is
160 concurrently subject to relative amplification specific to any point on the surface. We first
161 provide the theoretical physical basis for the decomposition and then describe the simulation
162 domain and the numerical scheme used to explore it. We then describe how the main elements of
163 the problem, i.e., regional mean field attenuation (Δ) and local site-specific amplification (A)
164 (explained in the subsequent section), can be extracted from the simulations and demonstrate
165 their use in the reconstruction of originally simulated intensities. We highlight that the
166 assessment of these reconstructed intensities is not notably influenced by source characteristics

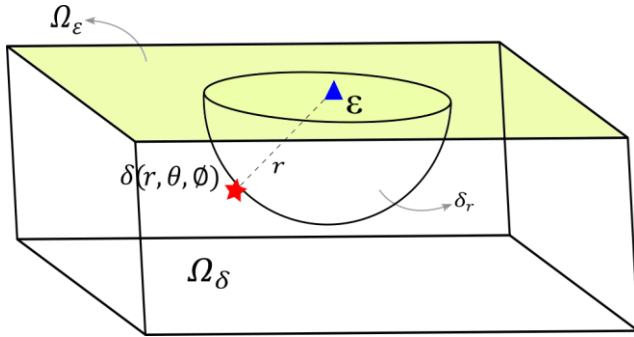
167 (such as location and directivity). Therefore, calibrating these parameters and understanding
 168 short-scale ground motion amplification variability can address the challenge posed by the lack
 169 of earthquake data. We suggest that this approach, when extended to including Higher
 170 Frequencies (HF), might provide an improved relative seismic risk assessment in the form of
 171 more reliable microzonation maps at the scale of urban planning, which is based on rapid
 172 seismological site characterization in the absence of long duration seismic catalogues.

173 2 Theoretical considerations

174 Using the seismic representation theorem, (De Hoop, 1958; Knopoff, 1956), in polar coordinates
 175 the displacement $\mathbf{U}_{\delta,\varepsilon}$ recorded at a site ε for a point-source earthquake δ is given by:

$$176 \quad \mathbf{U}_{\delta,\varepsilon} = \mathbf{G}_{\delta(r,\theta,\phi),\varepsilon} * \mathbf{f}_{\delta(r,\theta,\phi)} \quad (2)$$

177 Where, \mathbf{r} is the distance between source and receiver, and θ and ϕ are the positional angles in a
 178 spherical coordinate system, \mathbf{f}_{δ} is a force vector at δ and \mathbf{G} is the elastodynamic Green's
 179 function providing the displacement at ε due to \mathbf{f}_{δ} . Since we consider the peak displacement in
 180 elastic medium in what follows, this equation is time invariant.



181
 182 *Figure 1: A cuboidal domain having a receiver at ε and a seismic point source at $\delta(\mathbf{r}, \theta, \phi)$. The*
 183 *top surface of this domain represents receiver field Ω_ε and the volume defines a source field Ω_δ .*
 184 *All sources at a distance \mathbf{r} from ε can be represented as the surface of hemisphere δ_r . These*
 185 *ground motion intensity at ε due to these sources are integrated in equation 3. This can further*
 186 *be integrated for all receivers at the surface Ω_ε , as calculated in equation 4.*

187 Consider a receiver at point $\boldsymbol{\varepsilon}$ that experiences displacements due to sources of a given seismic
 188 moment at a point $\boldsymbol{\delta}$ (see Figure 1). The average logarithm of the peak displacement field for all
 189 possible point sources $\boldsymbol{\delta}_r$ at distance r from the receiver $\boldsymbol{\varepsilon}$ can then be expressed as-

$$190 \quad \overline{\ln(U_{\boldsymbol{\delta}_r\boldsymbol{\varepsilon}})} = \frac{1}{2\pi^2} \int_0^\pi \int_0^{2\pi} \ln(U_{\boldsymbol{\delta}(r,\theta,\phi),\boldsymbol{\varepsilon}}) d\theta d\phi \quad (3)$$

191 $\overline{\ln(U_{\boldsymbol{\delta}_r\boldsymbol{\varepsilon}})}$ then represents the expectation value for the intensity at $\boldsymbol{\varepsilon}$ due to all possible events at
 192 distance r . In this formulation, we consider point sources without any particular focal
 193 mechanism, so equation 3 might be considered as an integration over all possible focal
 194 mechanisms at all possible points on the hemisphere.

195 Integrating over all receivers $\boldsymbol{\Omega}_\varepsilon$ on the surface of the domain:

$$196 \quad \overline{\ln(U_{(\boldsymbol{\delta\varepsilon})_r})} = \frac{1}{\boldsymbol{\Omega}_\varepsilon} \iint_{\boldsymbol{\Omega}_\varepsilon} \overline{\ln(U_{\boldsymbol{\delta}_r\boldsymbol{\varepsilon}})} d\boldsymbol{\varepsilon} \quad (4)$$

197 then provides a mean field estimate of the expected intensity for any source-receiver pair
 198 separated by the distance r , and a graph of $\overline{\ln(U_{(\boldsymbol{\delta\varepsilon})_r})}$ against r , represents the mean field decay
 199 of intensity with distance throughout the entire volume.

200 The response at a particular location on the surface to any specific event at some distance r will,
 201 of course, be subject to the source, path and site effects, all contributing to some local
 202 modification of the mean field expectation. Consider the ground motion at a receiver $\boldsymbol{\varepsilon}$ due to
 203 any source $\boldsymbol{\delta}$, again, the peak displacement ($U_{\boldsymbol{\delta},\boldsymbol{\varepsilon}}$) can be calculated using the representation
 204 theorem, this time giving:

$$205 \quad U_{\boldsymbol{\delta},\boldsymbol{\varepsilon}} = \mathbf{G}_{\boldsymbol{\delta},\boldsymbol{\varepsilon}} * \mathbf{f}_\boldsymbol{\delta} \quad (5)$$

206 This peak ground displacement $U_{\boldsymbol{\delta},\boldsymbol{\varepsilon}}$ varies with $\boldsymbol{\varepsilon}$ but from Equation 4, we know its mean across
 207 the surface is $\overline{\ln(U_{(\boldsymbol{\delta\varepsilon})_r})}$. Normalising the $U_{\boldsymbol{\delta},\boldsymbol{\varepsilon}}$ by $\overline{\ln(U_{(\boldsymbol{\delta\varepsilon})_r})}$ removes the mean field decay
 208 leading to a normalised displacement $\widehat{U}_{\boldsymbol{\delta},\boldsymbol{\varepsilon}}$ given by:

209
$$\widehat{U}_{\delta,\varepsilon} = \frac{U_{\delta,\varepsilon}}{\ln(U_{(\delta\varepsilon)_r})} \quad (6)$$

210 Finally, to encapsulate the effect of all possible sources at each receiver, this normalised
 211 displacement can be integrated for the entire source field (Ω_δ),
 212 giving:

213
$$\overline{\ln(\widehat{U}_\varepsilon)} = \frac{1}{\Omega_\delta} \iiint_{\Omega_\delta} \ln(\widehat{U}_{\delta,\varepsilon}) d\delta \quad (7)$$

214 This $\overline{\ln(\widehat{U}_\varepsilon)}$ describes a local normalised amplification expected at any point for all possible
 215 sources. This can be considered as the integrated effect of the whole wave path from all possible
 216 sources that is dominated near ε where these paths converge. This term introduces the empirical
 217 site-specific variability using the normalised intensity of a suite of earthquakes of any magnitude.

218 Equations 4 and 7 now allow us to express the final estimate of intensity measure as:

219
$$\ln(IM) = \overline{\ln(U_{(\delta\varepsilon)_r})} + \overline{\ln(\widehat{U}_\varepsilon)} \quad (8)$$

220 For the sake of simplicity, for an event at i , observed at a location j , separated by a distance r ,
 221 $\ln\Delta_r$ is used to denote the first term, the mean intensity decay $\overline{\ln(U_{(\delta\varepsilon)_r})}$ and $\ln A_j$ defines the
 222 second term describing amplification, $\overline{\ln(\widehat{U}_\varepsilon)}$. Now, equation 8 can then be re-written as:

223
$$IM_{i,j} = \Delta_r * A_j \quad (9)$$

224 Where IM_{ij} is a non-specific intensity measure recognising that the argument so far may be
 225 generalised to peak velocity or acceleration. IM_{ij} then, provides an estimate of the intensity of
 226 ground motion based on the mean field expected intensity at a distance Δ_r , integrated over the
 227 entire crustal volume under consideration, and a relative amplification A_j due to the integrated
 228 effect of the seismic velocity structure around the site. Both terms on the right hand side are
 229 properties of the crust, regionally and locally, and do not include extended descriptions of the
 230 earthquake source, as we show in the next section. Equation 9 defines the $\Delta - A$ decomposition,
 231 a static ground motion model that emphasises local geology rather than the descriptions of the
 232 earthquake source.

233 In practice, the mean field Δ and amplification \mathbf{A} , can both be calibrated through simulation
234 based estimates for a given domain, hence the basis is essentially non-ergodic, but it is different
235 than data-based statistically estimated parameters used in typical non-ergodic GMM (e.g.
236 Landwehr *et al.*, 2016; Kuehn, Abrahamson and Walling, 2019). The spatial coefficients
237 estimated in these non-ergodic model are data-dependent, hence in order to find potential drivers
238 of GM variability in data sparse regions, there is very little scope to use these models. To clarify,
239 the motivation for the potential utility of Δ - \mathbf{A} method is to target the data-sparse regions without
240 extensive availability of earthquake catalogues.

241 **3 Defining Domain and source scenarios for simulations**

242 To explore the behavior and stability of Δ and \mathbf{A} (in equation 9) and how they might be estimated
243 in practice, we use a virtual world that allows the exploration of the ideas in the absence of
244 uncertainty but which allows the introduction of precisely constrained variability. We use a
245 virtual crustal environment, as shown in Figure 2 (a,b), that incorporates a simplified subsurface
246 velocity structure centered on a shallow and a deep river basin overlying a crystalline basement
247 to which simplified velocities have been assigned. The description of the domain includes depth
248 varying density (ρ), shear wave speed (V_s), primary wave speed (V_p), and anelastic
249 attenuation factors (Q_p, Q_s), and is determined based on the assumed values of these parameters
250 at the surface of the shallow basin (river channel), deep basin and basement (Brocher, 2005,
251 2008). The reader is referred to the Jenkins *et al.*, 2023, section 3.1 for detailed description for
252 crustal domain and earthquake moment distribution. Alternatively, this information is also
253 accessible in the supplementary materials (Table S1 and Figure S1).

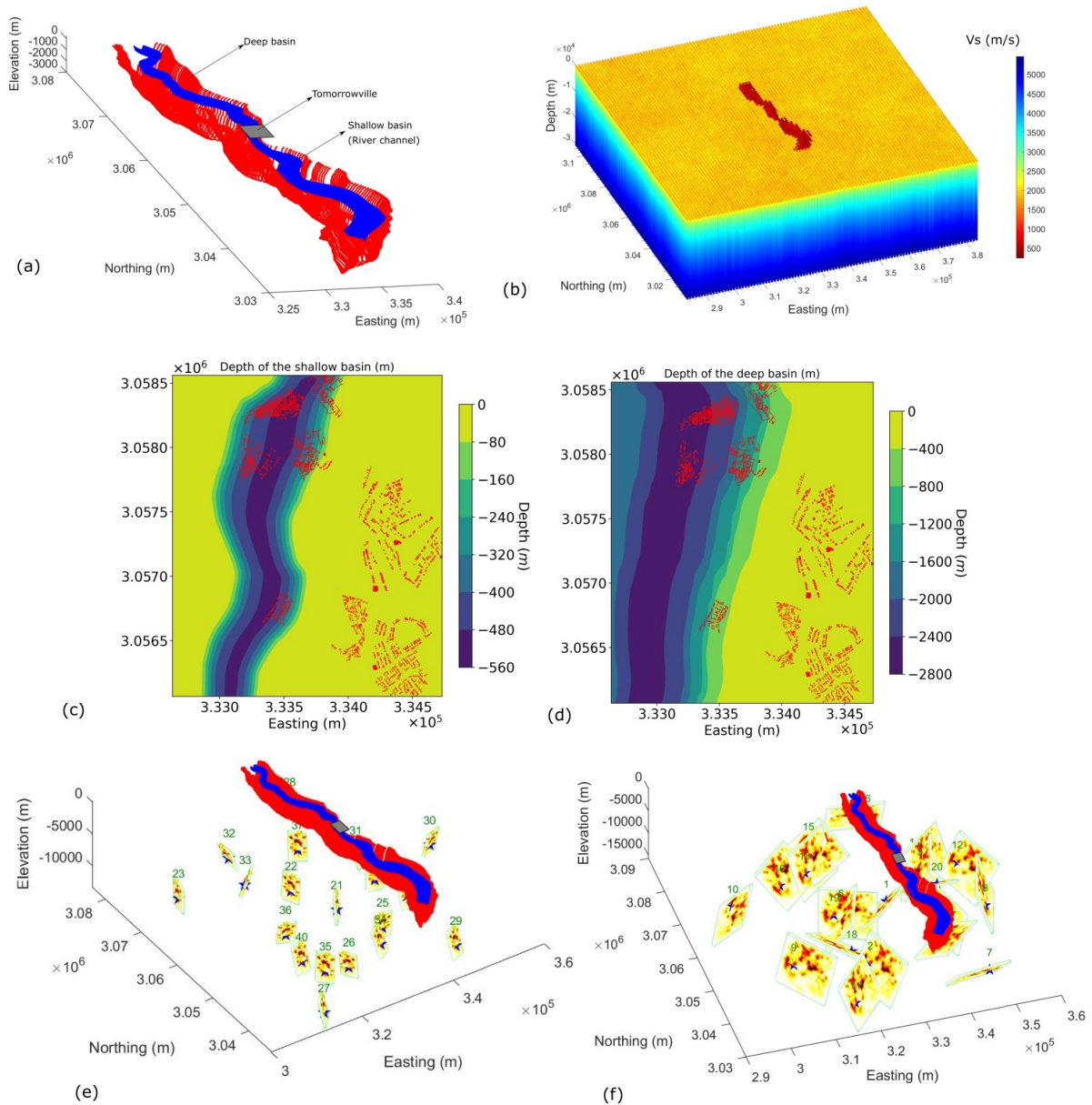
254 In the middle of crustal domain, we locate a virtual urban environment Tomorrowville (Cremen
255 *et al.*, 2023; Gentile *et al.*, 2022; Jenkins *et al.*, 2023; Menteşe *et al.*, 2023; C. Wang *et al.*, 2023).
256 The geology of Tomorrowville is based on a stretch of the Nakhu river valley on the outskirts of
257 Lalitpur to the south of Kathmandu though the velocity structure described here extends far to
258 the north and south, and does not represent the actual subsurface seismic velocity in the area.
259 Instead, we simply generate a hypothetical near-surface velocity structure representative of any

260 urban settlement located around a river channel set in a deeper and wider sedimentary basin. The
261 depths of shallow and deep basins in Tomorrowville are presented in Figure 2 (c,d).

262 The random distribution of 40 thrust-faulting earthquakes (EQ1 to EQ20 are **Mw6** and EQ21 to
263 EQ40 are **Mw5**) is simulated across the domain (see Figure 2 e,f) using an established physics
264 based solver, SPEED, which uses Spectral Element Method (SEM) for solving the wave-
265 propagation equations (Mazzieri, Stupazzini, Guidotti, & Smerzini, 2013; Paolucci et al., 2014;
266 Smerzini et al., 2011). The SEM combines the geometrical flexibility of the Finite Elements
267 Method (FEM), i.e., the capability to naturally account for irregular interfaces and mesh
268 adaptivity, with the high spectral accuracy, i.e., the exponential convergence rate to the exact
269 solution that results in a fewer number of grid points per wavelength to maintain low dispersion.
270 The crustal domain has a minimum shear wave velocity of 250 m/s and the smallest element size
271 of 200m with the spectral degree of 4, hence, the simulations are able to resolve for the
272 vibrational periods greater than 0.8s. Fault plane dimensions are determined using widely used
273 empirical relationships developed by Wells & Coppersmith, 1994. Kinematic characterisation of
274 rupture model is done based on the model developed by Liu et al., 2006; Schmedes et al., 2013 in
275 which the correlation between the slip, rise time, peak time and rupture velocity among the sub-
276 faults are derived based on a large ensemble of dynamic rupture simulations of dipping faults.
277 The moment distribution remains same for each magnitude ensemble, but the strike and dip are
278 varied. This distribution of rupture scenarios produce a wide range of expected source directivity
279 for any location. The Peak Ground Acceleration (PGA) maps shown in Figure S2 and Movie S1,
280 are referred for the visualisation of source orientation and their corresponding effects across the
281 surface of entire domain. The wavefront evolution for EQ1 can also be found in Movies S2, S3
282 and S4 of the supplementary information as well.

283 The Δ -**A** decomposition, developed theoretically above (Section 2), includes no source
284 variability whereas any attempt to understand seismic hazard must. The azimuth of the events
285 from the seismometer with respect to the dominant velocity anisotropy introduced by the river
286 basin will also contribute to the expected ground motion variability. The aim of this manuscript
287 is not to examine the influence of these features on the observed local intensity; that will follow
288 in a later work. Instead, we simply explore the extent to which the relative amplification term,
289 A_j , might act as a usable proxy that, to first order, governs the intensity variation across an urban

290 area, irrespective of the source orientation. This might be considered as a lower bound on the
 291 skill of equation 9 in providing the basis for a static site-dependent ground motion model that
 292 might be improved later by the introduction of a source term to be constrained by the structural
 293 fabric and stress state around any specific location.



294

295 *Figure 2: The computational domain used for the simulations and the distribution of earthquake*
 296 *scenarios is shown. a) The sedimentary basin structure showing a river channel creating a*
 297 *shallow basin of maximum depth 500m located inside a 2km deep basin (see Jenkins et al., 2023*

298 *for details). The gray rectangle represents Tomorrowville (eg. Cremen et al., 2022, Mentese et*
 299 *al., 2022), which has been designed to help understand the implications of development decision*
 300 *making on consequent risk to future communities. b) Represents the extent of the basin*
 301 *geometries using the shear wave velocities in a crustal volume of dimensions 100 km in length,*
 302 *100km in width and 30km in depth. c) and d) show the basin depths of shallow and deep basins*
 303 *across Tomorrowville with buildings distribution (red polygons). The building distribution is*
 304 *shown to highlight the direct impact of seismicity across the potential future infrastructure. e)*
 305 *and f) show 40 thrust earthquakes with random distributions of dip, rake and strike with EQ21 to*
 306 *EQ40 of Mw5 and EQ1 to EQ20 of Mw6 are generated across the domain. The hypocentres*
 307 *are represented by blue stars on the fault surface. The colour distribution across each rupture*
 308 *surface shows the moment release following the kinematic rupture models as developed by Liu et*
 309 *al., 2006; Schmedes et al., 2013.*

310 **4 Estimation of Δ and A for Tomorrowville**

311 The simulation results are used to estimate the Δ for the crustal domain and A for Tomorrowville
 312 (equation 9). The geometric mean of horizontal components of PGA values are used as intensity
 313 measure for all of the rupture scenarios.

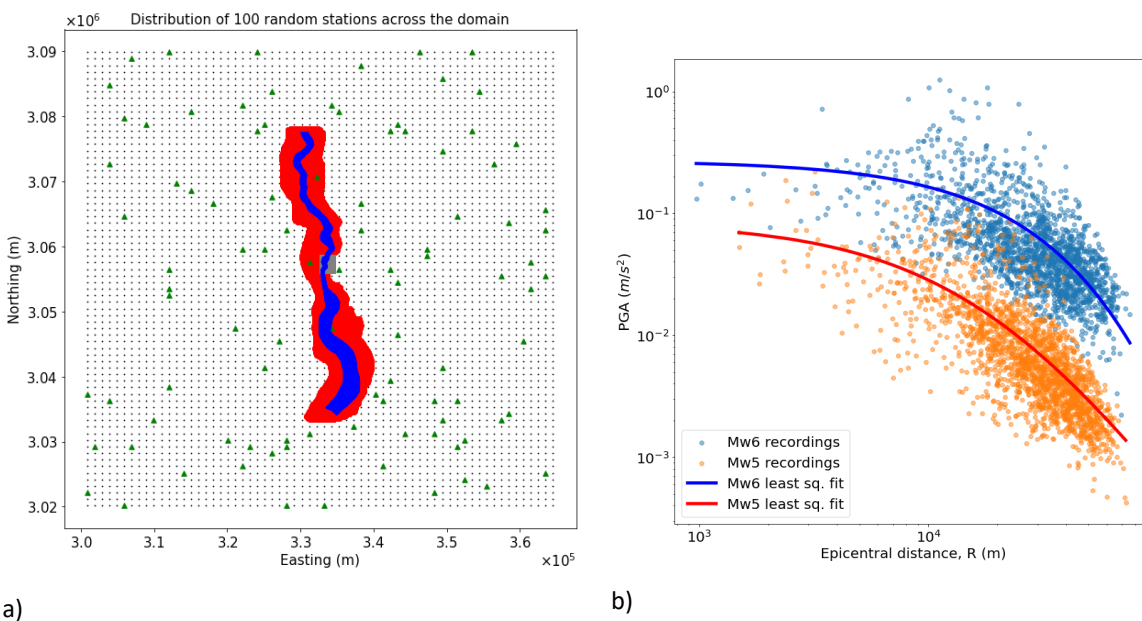
314 To calculate Δ , we uniformly sample the surface of crustal domain which is a practical and
 315 computationally inexpensive approach to approximate the integration in equation 4. In the entire
 316 simulation domain, a random set of 100 recording locations is chosen (see green triangles in
 317 Figure 3a) for which estimates of the PGA are simulated for every event, generating a large
 318 number of estimates of the peak amplitude for different epicentral distances giving the data
 319 points for magnitude 5 and 6 events shown in Figure 3b. We use simple least squares regression
 320 to the decay equation:

$$321 \quad |\Delta_r| = a + b \times \ln(r + c) \quad (10)$$

322 here, $|\Delta_r|$ is an estimation of the mean field intensity measure Δ_r (introduced in equation 9), r is
 323 the epicentral distance and a,b and c are the empirical parameters evaluated from the data fitting
 324 procedure which might be modified without loss of insight (Figure 3b). The choice of 100
 325 recording locations for $|\Delta_r|$ estimation can have inherent uncertainties based on the selection.
 326 For instance, if the stations are predominantly concentrated in the basin, it could result in higher

327 intensities in Figure 3b, consequently causing an upward shift in the mean field curve. However,
 328 such a scenario would not uniform sample the entire domain as intended; hence, current choice
 329 of stations seem satisfactory.

330 It should be noted that the regression method chosen here does not distinguish the repeatable
 331 (within event) and non-repeatable (between events) effects, which is followed from the fact that
 332 each source used here is characteristically similar and is recorded at the exact same set of
 333 receivers. Assuming the entire domain has a homogeneous earthquake distribution, each
 334 recording is considered independent, irrespective of whether the seismic energy is originated
 335 from same or different sources. The concept of earthquake source homogeneity implies that in a
 336 scenario with limited prior knowledge of the tectonics in the area, a reverse faulting earthquake
 337 could potentially occur at any azimuth with respect to the city.



338 *Figure 3: a) A map of the computational domain showing the shallow basin (blue) created by*
 339 *river channel, and a deep basin (red), as well as the location of Tomorrowville (gray). Green*
 340 *triangles indicate the random locations of the 100 virtual seismometers. b) points indicate PGA*
 341 *versus epicentral distance for each of the 40 events at each virtual seismometer and the curves*
 342 *represents the least squares estimate of the mean field amplitude decay for this data.*

343 We now must turn our attention to the variability of the data around the curves (Figure 3b) and
 344 will focus on the Tomorrowville sub-domain. Note, any numerical uncertainties due to the

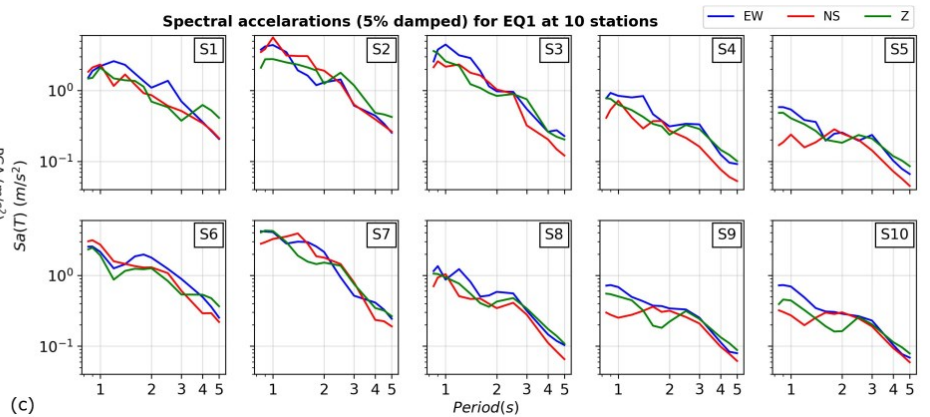
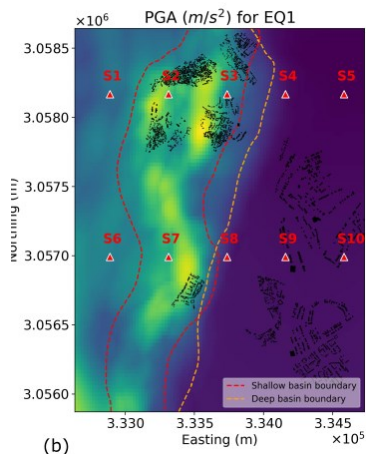
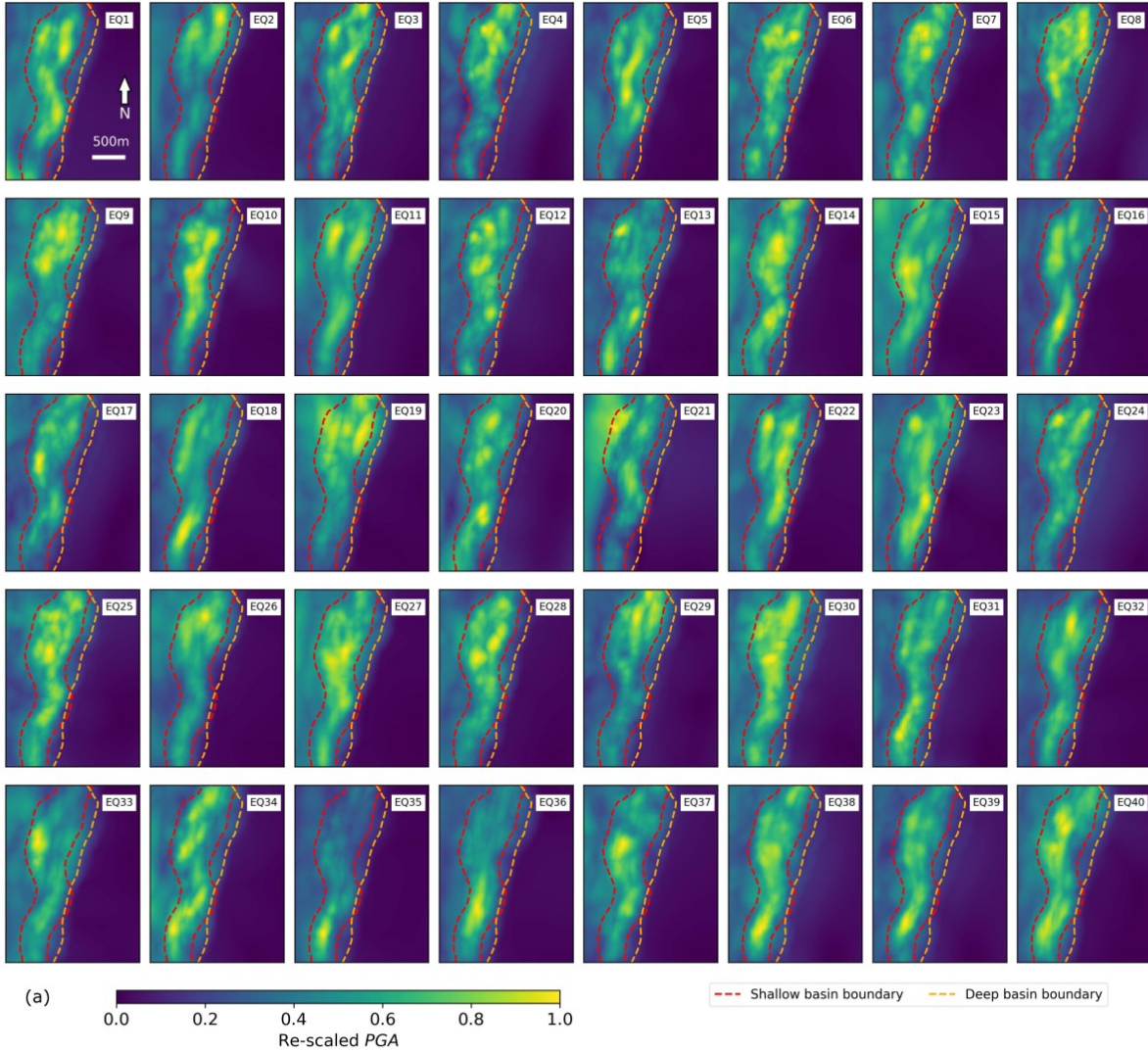
345 calculation, conditional on the input geological structure, are negligible compared to the
346 variability observed in Figure 3b. Hence, given the assumption that the simulation is providing
347 accurate estimates in a virtual setting, each point in Figure 3b accurately represents the local
348 peak amplitude of waves from a particular event recorded at a single station. To estimate $|A_j|$
349 for any location j , the PGA values from all events are extracted for the Tomorrowville domain
350 (Figure 4a). Linear interpolation of intensities are used to provide these high-resolution maps,
351 which sample Tomorrowville at an approximate grid spacing of 28 meters.

352 As an example, PGA from earthquake 1 (EQ1) is shown along with the spectral accelerations
353 (5% damped) at 10 stations, S1 to S10 (Figure 4b,c). Please note that these receivers are
354 positioned within the Tomorrowville domain and are not accounted for in the wider receiver
355 distribution illustrated in Figure 3a for the evaluation of $|\Delta_r|$. It can be clearly seen that the basin
356 area is showing strong amplification resulting in higher PGA values due to wave trapping and
357 resonance of the sedimentary basin layers, as compared to the lower PGA values along the areas
358 of crystalline basement. Spectral accelerations at 10 stations show different orders of
359 amplification over the entire period range (0.8s to 5s) corresponding to the geological locations
360 of these stations. The consistent decrease in amplitude with increasing period observed at all
361 stations indicates that it is majorly controlled by the selected source spectra. Stations S2, S3 and
362 S7 lie in the combined (both deep and shallow) basin area and hence, recording maximum
363 amplification, while the stations S1 and S6 lie above only deep basin area, hence the
364 amplification is lesser but still significant at higher periods for all three components. The rest of
365 the stations, S4, S5, S9 and S10 are situated over the basement rocks, hence recording the lowest
366 value of spectral accelerations.

367 Our simulations focus on frequencies below 1Hz due to high computational costs associated with
368 sampling higher frequencies in simulations. However, this analysis remains relevant since basins,
369 like the Kathmandu basin, often exhibit resonance at similar frequencies (Asimaki et al., 2017;
370 Oral et al., 2022). Additionally, when dealing with higher frequencies, it becomes necessary to
371 account for other non-linear site effects that play a significant role in intensity variations

372 (Semblat et al., 2005), which are not included in this analysis. More discussion on basin
 373 resonance is provided in the supplementary material Text S1.

Re-scaled PGA maps for 40 earthquakes across Tomorrowville



374

375 *Figure 4: a) PGA maps for 40 events plotted on Tomorrowville city domain. EQ1 to EQ20*
376 *represent data from Mw6 earthquakes while EQ21 to EQ40 are for Mw5. Note that we have*
377 *scaled each map between 0 and 1, where 0 is minimum and 1 is maximum PGA for each*
378 *earthquake. The similarity of the maps indicates that, to first order, regardless of the absolute*
379 *value of the PGA across the zone, the relative amplitude for different locations is invariant. b)*
380 *Shows the PGA (geometric mean of two horizontal components) values for EQ1 along with the*
381 *boundaries of shallow and deep basins, represented by red and orange dashed lines,*
382 *respectively. Red triangles show 10 stations, S1 to S10 that are used to show the spectral*
383 *accelerations for the 0.8s to 5s in c). Three components East-West (EW), North-South (NS) and*
384 *Vertical (Z) are plotted separately.*

385 Given the geometry of the basin stretched approximately North-South (NS) whilst being much
386 more confined along East-West (EW), the amplification of both horizontal components should
387 be theoretically contrasting. However, the periods resolved in the simulations show the inter-
388 component variability is still lower than the inter-station variability across different geological
389 domains (Figure 4c). This suggests, the geometric mean of the horizontal components of PGA at
390 each station seem a usable guide to explore the amplification further discussed in this study.

391 The pattern of higher amplification along the river basin and lower amplification along the
392 basement area is common for PGA maps of all the earthquake scenarios (Figure 4a). Hence
393 while the absolute PGA is strongly dependent on the source magnitude and distance, the *relative*
394 amplitude within any map is qualitatively independent of earthquake source orientation, and
395 even magnitude. The structural similarity of PGA maps in Figure 4a seems to indicate the
396 potential utility of the $\Delta\text{-}\mathbf{A}$ decomposition.

398 To extract this pervasive feature of relative amplification from all earthquake scenarios we
399 normalise and stack the PGA maps for each event. First, all PGA maps are normalised using the
400 mean smooth earth expectation value $|\Delta_r|$, calculated from equation 10. This normalisation is the
401 practical implementation from the theoretical description given in the equation 6, where the
402 normalisation factor is taken as the mean intensity decay in equation 4. Let, $|\mathbf{U}_{ij}|$ be the

403 simulated PGA at a particular site j due to an earthquake i at a distance r , then the normalised
 404 PGA $|\widehat{U}_{ij}|$ would be –

$$405 \quad |\widehat{U}_{ij}| = |U_{ij}| / |\Delta_r| \quad (11)$$

406 After normalisation, the average PGA of the normalised maps is calculated for N_e number of
 407 earthquake scenarios, as described in equation 7. This final, averaged PGA map is a
 408 characteristic spatial kernel for the chosen city domain and theoretically contains the average
 409 local amplification (A_j) at any site j for any possible earthquake regardless of source, (see Figure
 410 5a). Here, A_j has the following form-

$$411 \quad A_j = \left(\prod_{i=1}^{N_e} |\widehat{U}_{ij}| \right)^{\frac{1}{N_e}} \quad (12)$$

412 The calculation of A_j results in a mean amplification field consistent with the spatial variations
 413 observed in the simulations (Figure 5a). Each pixel represents the mean amplification
 414 experienced at that location over all magnitudes, azimuths and directivity.

415 There is, of course, a dispersion of $\ln|\widehat{U}_{ij}|$ values around this mean which is itself a spatially
 416 variable field over the domain, calculated by the $\sigma_{\ln|\widehat{U}_{ij}|}$ (Figure 5b) as:

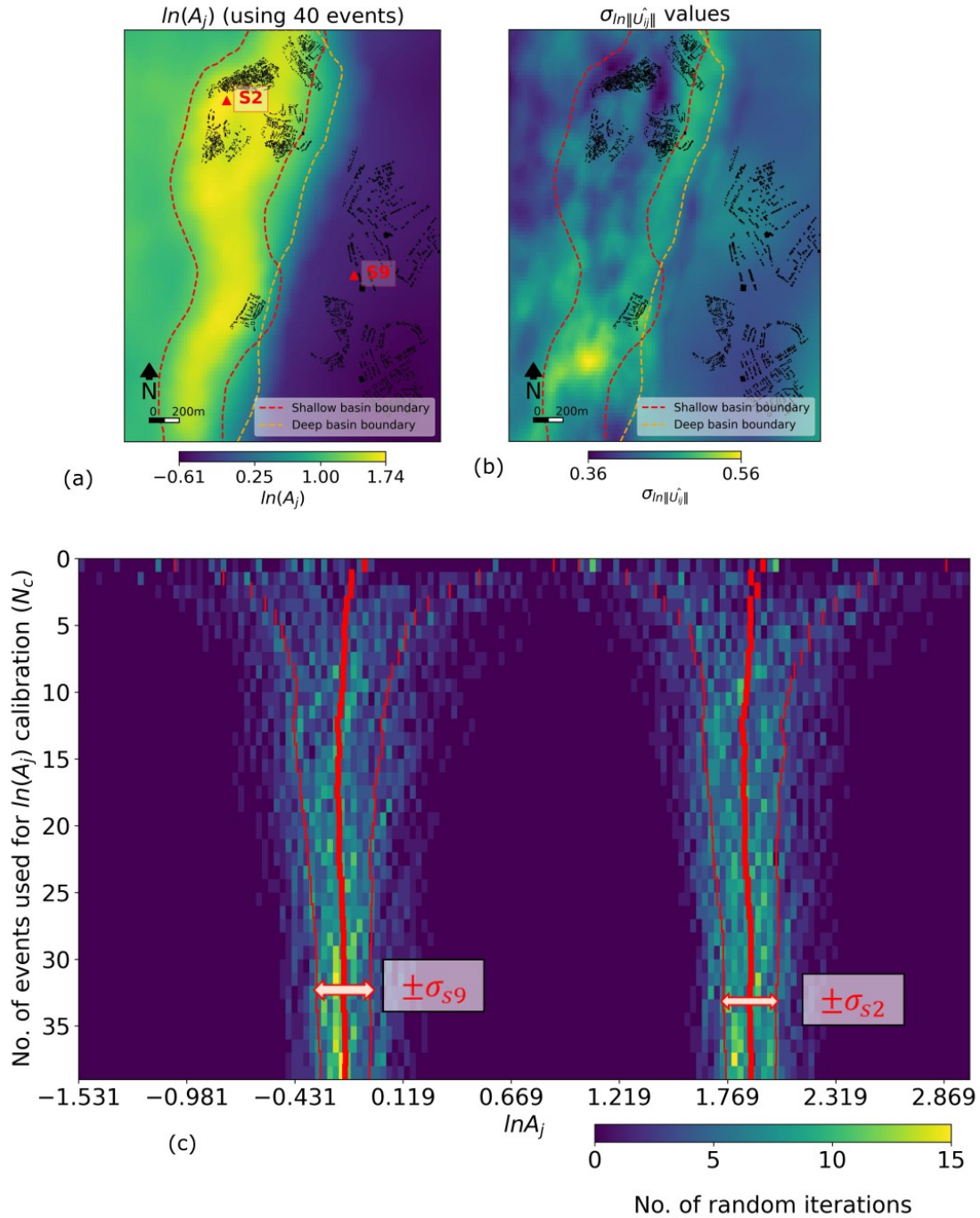
$$417 \quad \sigma_{\ln|\widehat{U}_{ij}|} = \sqrt{\frac{1}{N_e} \sum_{i=1}^{N_e} (\ln|\widehat{U}_{ij}| - \ln A_j)^2} \quad (13)$$

418 where, $\sigma_{\ln|\widehat{U}_{ij}|}$ gives the variability due to various source scenarios used in the analysis and the
 419 corresponding path effects. The maximum value of $\sigma_{\ln|\widehat{U}_{ij}|}$ is 0.56, that is 23.8% of the entire
 420 $\ln A_j$ range of 2.35 in Tomorrowville. The difference of 2.35 in maximum ($\ln A_{j,max}$) and
 421 minimum ($\ln A_{j,min}$) values would mean, the ratio $A_{j,max} / A_{j,min}$ is $e^{2.35} \sim 10.48$, implying an
 422 order of magnitude variation within Tomorrowville. Notably, the ranges of the amplification and

423 standard deviations are of a realistic order often found in some of the extensively studied real-
424 world settings as well, for example as shown by Day et al., 2019 in Southern California.

425 Another approach to understanding the variability of the amplification field involves varying the
426 number of events used to calculate $\ln A_j$ and examining its variability at a specific location using
427 the events selected through a bootstrapping approach. We chose two stations from Figure 4b, one
428 representing an area of high amplification over the river basin, named as **S2**, and one in low
429 amplification over outcropping basement, named as **S9** (see Figure 5a). The number of events
430 N_c , used to estimate A_j , is plotted against the $\ln A_j$, where the colour intensity represents the
431 distribution of the iterations across the entire $\ln A_j$ range (Figure 5c). For each N_c value, 100
432 random combination of events with repetition are used for $\ln A_j$ calculation. The red dashes
433 correspond to the $\pm 1 \sigma_{s2}$ and $\pm 1 \sigma_{s9}$ variability around the mean $\ln A_j$ value for the respective
434 N_c value. The convergence of the $\ln A_j$ values can be observed even with as low as ~ 7 events
435 with a stable $\pm \sigma_{s2}$ and $\pm \sigma_{s9}$ around the $\ln A_j$ values of 0.12 each. This distribution of $\ln A_j$ is
436 non-overlapping for both sites, **S2** and **S9**, which suggests that the local crustal features at both
437 of these sites is the dominant contributor in the amplification.

438



439

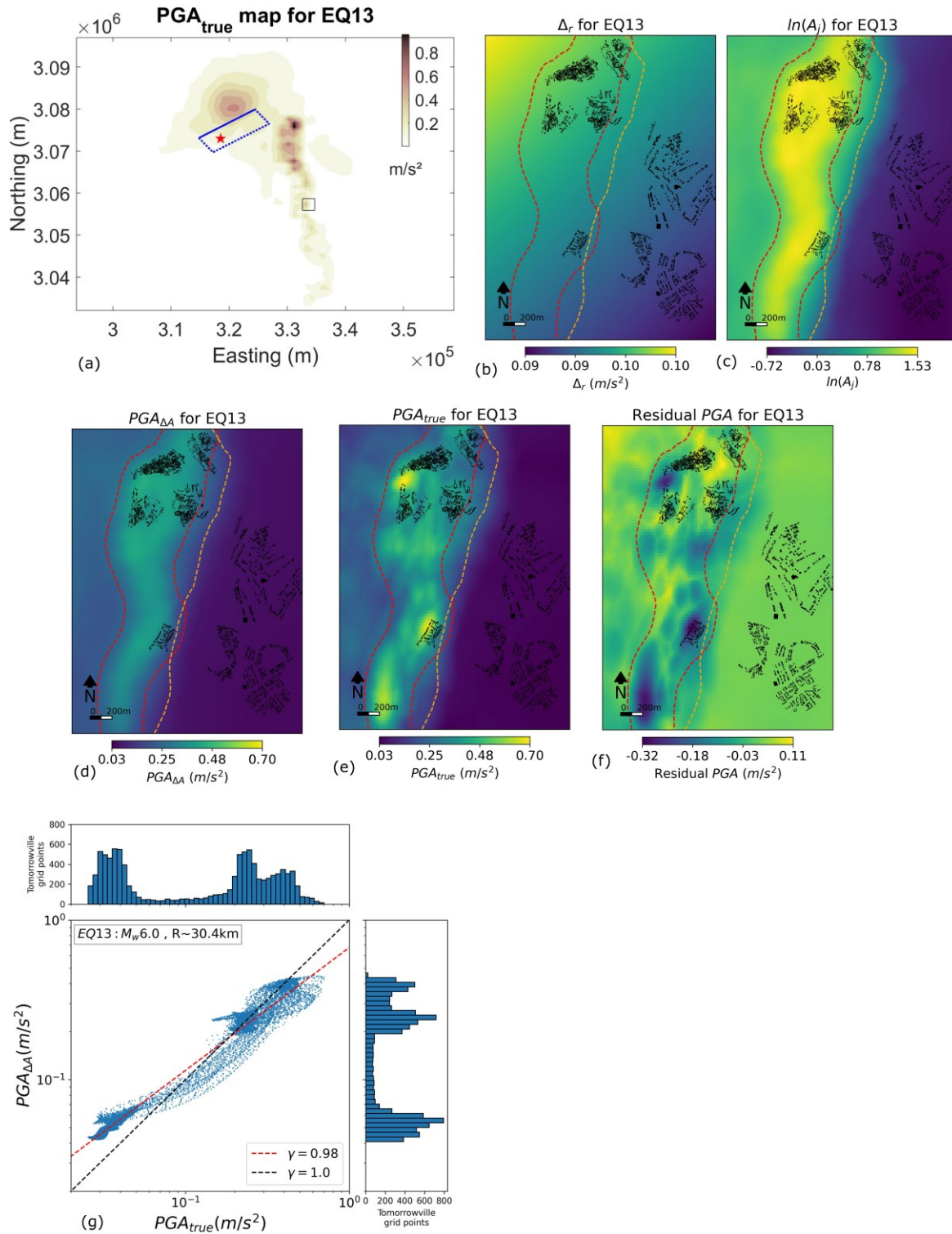
440 Figure 5: a) Estimates of $\ln A_j$, and b) the standard deviation ($\sigma_{\ln|\hat{U}_{ij}|}$) for Tomorrowville. Two
 441 locations, one in the river basin (**S2**), and one where the crystalline basement outcrops at the
 442 surface at (**S9**) are chosen in a), to plot the convergence of the $\ln A_j$ at **S2** and **S9** with an
 443 increasing number of events as shown in c).

444 5 Estimation of PGA using Δ and A for 40 earthquakes

445 The theoretical treatment described in section 2 above suggests that the ground motion at a point
446 can be decomposed into the effect of the mean field attenuation over the wave path integrated
447 over the crustal volume and the effect of the local velocity structure. This implies that the
448 reversal of this process should reproduce the original PGA field. Thus if we have robust
449 estimates of Δ and A , then we should be able to reproduce the intensity at any point using
450 equation 9.

451 We demonstrate this process for a single earthquake, EQ13 located 30.4 km to the NW of
452 Tomorrowville, we will show that the choice of the earthquake is not important. The simulated
453 PGA at every point will be referred to as the true value, PGA_{true} (see Figure 6a,e). To estimate
454 the PGA value explained in equation 9 for this event, referred herein as $PGA_{\Delta A}$, we first calibrate
455 the Δ (Figure 6b) and A (Figure 6c) using the rest of 39 simulated events. Δ and A are multiplied
456 as shown in equation 9 to obtain $PGA_{\Delta A}$ values for this earthquake (see Figure 6d). The
457 difference between $PGA_{\Delta A}$ and PGA_{true} is calculated and plotted as a residual map (see Figure
458 6f). The basin area shows higher negative residuals suggesting underestimation of $PGA_{\Delta A}$ where
459 PGA_{true} values are higher, while surrounding basement exhibits positive values, suggesting
460 overestimation. A graph of $PGA_{\Delta A}$ as a function of PGA_{true} is shown in Figure 6g along with
461 the histograms of all the grid points across Tomorrowville. There is a systematic overestimation
462 of $PGA_{\Delta A}$ values for this particular event at the lower PGA range, and a minor underestimation
463 can be seen at the higher PGA side. This pattern can be attributed to the characteristic that the
464 $\ln A_j$ values, which are used to calculate $PGA_{\Delta A}$, have mean amplification values spanning a
465 wider range compared to this specific event. Pearson correlation coefficient (γ) between
466 logarithms of $PGA_{\Delta A}$ and PGA_{true} is 0.98, suggesting strong correlation between the two. The
467 histograms presented in parallel to the axes also indicate that the distribution nature of PGA
468 remains preserved across Tomorrowville, exhibiting a tri-modal pattern in both PGA_{true} and
469 $PGA_{\Delta A}$ (Figure 6g). This tri-modal pattern is a distinctive influence of three geological domains
470 in the city- the deep basin area (to the left of shallow basin boundary), the area comprising both
471 deep and shallow basins, and the basement region.

472



473

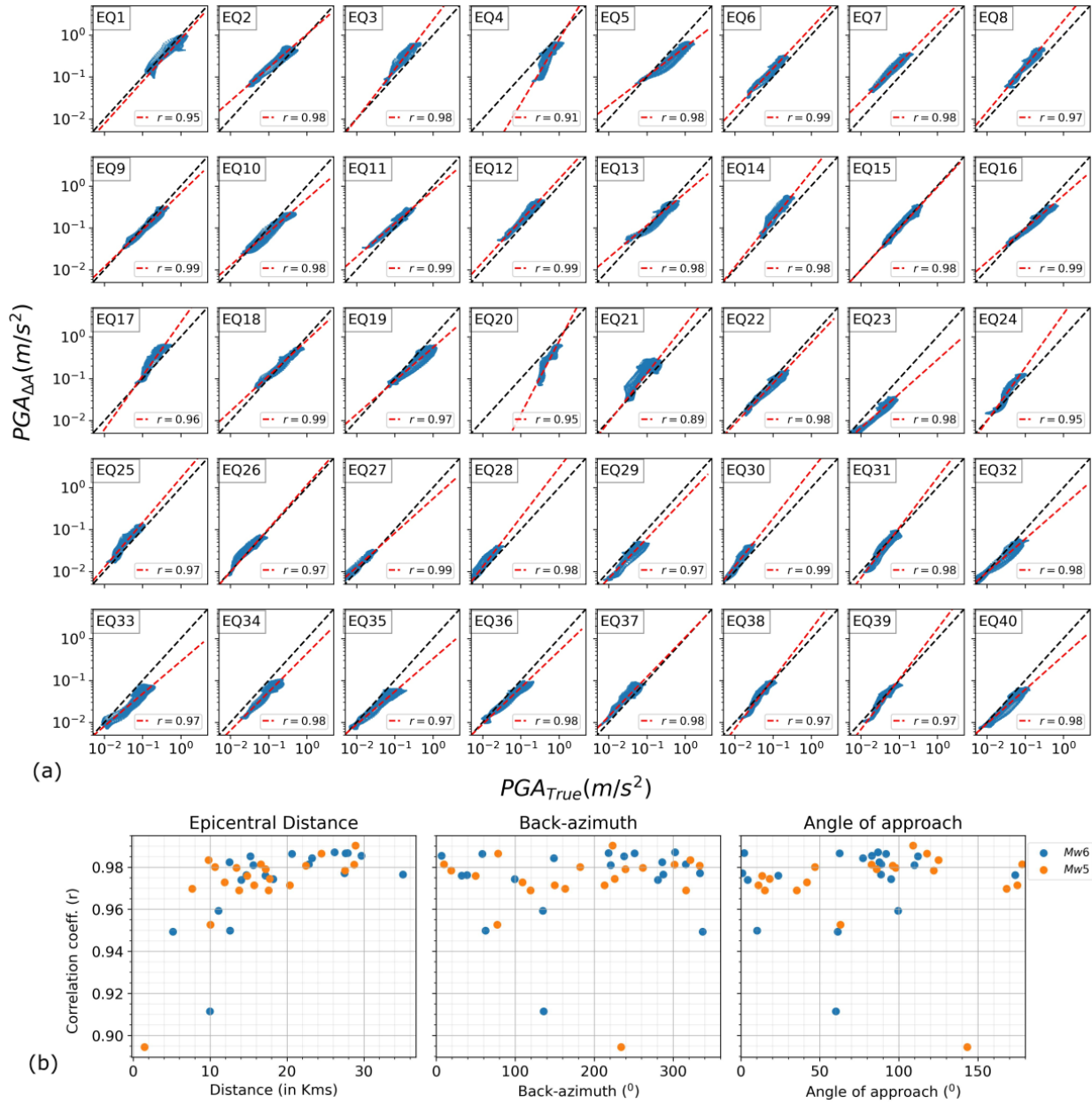
474 *Figure 6: Result showing estimated parameters for EQ13. a) PGA_{true} map for EQ13 showing*
 475 *the simulation results across the entire crustal domain, the blue dashed-rectangle shows the*

476 location of rupture surface (top edge is solid blue), red star shows the hypocentre and black
 477 rectangle in the middle of domain shows the location of Tomorrowville. b) shows Δ_r and c)
 478 shows $\ln \mathbf{A}_j$ for event EQ13 for Tomorrowville. d) shows the $\mathbf{PGA}_{\Delta A}$ distribution calculated by
 479 multiplying Δ_r with \mathbf{A}_j as conceptualised in equation 9. e) \mathbf{PGA}_{true} map for this event obtained
 480 through the PB simulation. f) residual between $\mathbf{PGA}_{\Delta A}$ and \mathbf{PGA}_{true} g) shows the comparison
 481 between $\mathbf{PGA}_{\Delta A}$ and \mathbf{PGA}_{true} for EQ13 using the Pearson correlation coefficient (γ) of 0.98 for
 482 this event. Marginal panels show histograms of $\mathbf{PGA}_{\Delta A}$ (right) and \mathbf{PGA}_{true} (top) indicating the
 483 similarity in distribution of \mathbf{PGA} values across Tomorrowville city domain.

484 Finally, for each event in the suite of 40 earthquakes, the remaining 39 simulations are used to
 485 calculate the Δ and \mathbf{A} , that are multiplied to obtain $\mathbf{PGA}_{\Delta A}$. The results are compared with the
 486 corresponding \mathbf{PGA}_{true} of each earthquake using the γ value and best fitting regression line
 487 (Figure 7a). Lowest γ value is 0.89, which suggests the correlation is strong for all the
 488 earthquakes. In conclusion, there is a clear potential of predictability in $\mathbf{PGA}_{\Delta A}$, with some
 489 variability translated from different source-specific variability due to heterogeneous moment
 490 distribution along the fault surface, as well as, path related variability due to azimuth of sources
 491 with respect to the Tomorrowville. This variability in $\mathbf{PGA}_{\Delta A}$, is captured earlier using the
 492 $\sigma_{\ln|\widehat{U}_j|}$ values calculated in Figure 5b.

493 The impact of source orientation on the obtained γ value is illustrated by examining three
 494 parameters: epicentral distance, back azimuth of the earthquake (bearing of the line joining
 495 hypocenter to the center of Tomorrowville), and the angle of approach (the azimuthal difference
 496 between the line connecting the hypocenter to the major fault asperity, and the line connecting
 497 the hypocenter to the center of Tomorrowville) (Figure 7b). The back-azimuth and angle of
 498 approach provide insights into the influence of horizontally anisotropic crustal domain and
 499 directivity effects resulting from variations in fault orientation relative to Tomorrowville,
 500 respectively. γ is observed to have a positive trend with epicentral distance indicating that the
 501 earthquakes closer to tomorrowville are poorly constrained by $\mathbf{PGA}_{\Delta A}$ compared to the ones
 502 farther away. It can also be seen that the chosen earthquake distribution samples a wide range of
 503 back-azimuth and angle of approach values, indicating a comprehensive representation of these

504 factors. γ does not show any notable trend with the these two factors, hence, their impact on
 505 estimating the distribution of PGA values across Tomorrowville is not substantial.



506

507 *Figure 7: $\mathbf{PGA}_{\Delta A}$ is calculated for all 40 earthquakes and compared with the simulated PGA*
 508 *values (\mathbf{PGA}_{true}). A) Shows the correlation between $\mathbf{PGA}_{\Delta A}$ and \mathbf{PGA}_{true} for all earthquakes,*
 509 *where red dashed line shows the line of best fit and black dashes show the $\gamma = 1$ line. The γ*
 510 *value is mentioned for all the earthquakes. B) Shows the γ value versus distribution of the*
 511 *following three parameters for all 40 earthquakes- epicentral distance, back-azimuth (bearing of*

512 *line joining hypocenter to the center of Tomorrowville) and angle of approach (the azimuthal*
513 *difference between the line connecting the hypocenter to the major fault asperity, and the line*
514 *connecting the hypocenter to the center of Tomorrowville).*

515 **6 Discussion and summary**

516 Estimates from UNDRR suggest that the number of people at risk from a major earthquake will
517 increase from some 370 million in 2020 to more than 850 million by 2050 (UN-Habitat, 2022).
518 Due to historically unprecedented rapid urbanization, these people will be increasingly
519 concentrated in urban centers; the same source estimates that by 2050 global urban population
520 will increase from the current 56% to around 68% with 95% of this growth happening in the
521 global south. Without a concerted effort at providing decision support for high cost-benefit risk
522 sensitive construction, ongoing urbanization in areas of high seismic hazard, will increase
523 disaster risk for millions.

524 That the intensity of seismic shaking varies at high spatial frequencies is graphically
525 demonstrated by large differences of seismic damage over very short distances in areas of
526 uniform building code (Bielak et al., 1999; see also Asimaki et al., 2012; Dolce et al., 2003;
527 Ohsumi et al., 2016; Sextos et al., 2018). What is less well known is the extent to which this
528 variability is the result of differences in the earthquake source, or in contrasts in the rheological
529 properties of the near surface that might impose a stable and estimable LF amplification, to first
530 order independent of that source. The former prioritizes forecasting likely earthquake sources in
531 seismic hazard assessment, while the latter suggests that measuring the properties of the near
532 surface might produce a pathway to understanding spatial patterns of seismic shaking regardless
533 of the source. This would in turn open a path to the development of physics-based, high-
534 resolution building-code classification and support evidence based seismic urban planning
535 policy.

536 Current methods for seismic hazard assessment require seismic catalogues built from long-term
537 deployment of large numbers of seismometers to calibrate ground motion models (Douglas,
538 2017; Douglas & Aochi, 2008; Douglas & Edwards, 2016a). The observed variability around
539 these models is assumed to be stochastic and statistical methods are used to provide the moments
540 of the emerging distributions leading to low spatial resolution estimates of seismic hazard. Over

541 most of the Global South such long-term data has not been collected nor is there any current
542 appetite for deploying dense networks of seismometers required for this assessment at the
543 resolution which would be required to guide seismic risk informed urban planning at actionable
544 scales.

545 In this study we have harnessed the potential of high resolution PB earthquake simulations to
546 explore the extent to which seismic intensity variability might be described by near-surface
547 geology and that relative seismic intensity is independent of the earthquake source. Do some
548 areas shake more than others, regardless of the earthquake? We exploit the certainty of a virtual
549 world, Tomorrowville, in which the rheology, described by the geometry of the seismic velocity,
550 is known everywhere, in which seismic sources are precisely described by kinematic models
551 (Graves & Pitarka, 2010; Schmedes et al., 2013), and in which wave propagation is perfectly
552 described by the wave propagation solver (SPEED) we use (Mazzieri et al., 2013). The choice of
553 software should not lead to any notable deviation from the results obtained in this study.

554 The study develops a Δ - A decomposition, that splits the seismic process into a mean-field
555 attenuation model, describing the amplitude decay with source-receiver distance, and an
556 amplification field, describing the integrated amplification of the entire wave path as experienced
557 at each point on the surface. We have shown methods for the estimation of the Δ model and for
558 the A field for Tomorrowville and demonstrated that their description can be used estimate the
559 true PGA field.

560 This study utilizes PB simulations in a virtual environment that shows a significant fraction of
561 the observed variability can be explained without categorizing them as stochastic. In the real
562 world, beyond these deterministic variations, stochastic elements of the process must be
563 considered separately. Moreover, it becomes important to classify uncertainties as aleatory or
564 epistemic, when the real data guides the model fitting and resulting deviations (Kiureghian &
565 Ditlevsen, 2009). However, in this study, PB simulation results are assumed to be devoid of any
566 modelling uncertainties (or aleatory variability) and they are treated as reproducible true
567 solutions in the analysis. Consequently, the deviations obtained in the results of Figure 7a are
568 fundamentally epistemological. The difference between the amplification map for any event and
569 the A field that determines the value of the local PGA, is precisely quantified and accessible.

570 Investigations show that the maximum standard deviation of the \mathbf{A} field is about 23.8% of the
571 $\ln A_j$ measured across the entire area, that includes the source and path dependent variability.
572 More importantly, analysis of the variability of the amplification value at any point, indicated
573 stable convergence from as few as 7 event simulations. Furthermore, comparisons of
574 amplifications at locations over the river basin with locations on basement in Tomorrowville,
575 produced stable, order-of-magnitude differences in amplification which converged rapidly and
576 which gave stable non-overlapping amplification estimates. Of course, both the stability and the
577 contrast in amplification are functions of the choice of velocity distribution but the choice of
578 model here was developed to reflect not uncommon velocity geometry not to accentuate
579 amplification contrasts. We expect that the general conclusions of this work are independent of
580 the details of the Tomorrowville velocity model.

581 We have not attempted to explore the variability of the amplification with the source parameters
582 and the initial results suggest that the influence is not likely to be strong. The main candidates,
583 source directivity and epicentral azimuth, expected to be dominant in the strongly anisotropic
584 velocity model used here, do not make an appreciable systematic contribution to the \mathbf{A} field.
585 Descriptions of active fault geometry and seismotectonics of Tomorrowville could impose a
586 source fabric introducing some systematic influence on the amplification field. Incorporation of
587 any such influence could only constrain the variability so the results described here might be
588 considered as a lower bound on the stability of the \mathbf{A} field. The primary factor influencing
589 ground motion amplification in this study is the basin geometry or buried topography, although
590 the impact of surface topography is also anticipated to significantly affect the amplification
591 pattern (García-Pérez et al., 2021; Geli et al., 1988; Lee et al., 2009; Poursartip et al., 2020). The
592 surface topography, often rich in high-resolution data, is the most straightforward to control, and
593 it is expected to contribute to the observed variability. Future research will concentrate on
594 investigating the influence of surface topographic features, in addition to buried topography, on
595 the amplification phenomenon.

596 The reconstruction of the simulated PGA fields provided further evidence of the efficacy of the
597 method. Using estimates of the Δ and \mathbf{A} components from a set of 39 simulations provided strong
598 correlations between true and inverted PGA fields for the 40th. Further, in keeping with the
599 observation of non-overlapping amplification values for basement and basin locations, places

600 with high shaking were broadly consistently high for all events, locations experiencing low
601 intensity shaking were also consistent across all events.

602 The results are suggestive of an underlying physical process in which small-scale LF *relative*
603 shaking intensity is controlled more by local geology than by source process. Given the
604 description of the relevant fields through simulations, each taking approximately a day on a
605 commonly available computer clusters (see Table S3 for simulation parameters and run time
606 estimates), it is feasible to estimate the entire PGA field ($PGA_{\Delta A}$) for an event of a specific
607 magnitude and location in milliseconds of computing time. At the minimum, this provides a
608 workflow through which normal probabilistic seismic hazard assessments, that require estimates
609 of PGA for thousands of events at each location, can benefit from the advances in physics based
610 simulations without the massive compute overhead that make these computations unfeasible at
611 present.

612 The stability of the relative amplification field together with the stable, order of magnitude
613 difference in PGA across the surface of Tomorrowville demonstrated in this study, points to
614 methods for high-resolution seismic hazard estimation based on understanding the static
615 properties of the near surface, rather than on the unpredictable properties of future earthquakes.
616 The challenge becomes a problem of measurement, rather than forecasting. There remains the
617 critical problem either of the elucidation of the velocity structure of the near surface (Sebastiano
618 et al., 2019), so the Δ and A fields might be estimated through simulation as in this paper, or the
619 direct estimation of the field by measurement of the intensity of shaking at high resolution in the
620 area of interest. To clarify again, this study explores only LF near-surface effects arising from
621 the presence of complex sedimentary basins and show their contribution in short-scale variability
622 in amplification. It is noteworthy that these LF effects are additional to the site effects related to
623 very-near surface (decameter) depths, which include nonlinear soil responses and other high
624 spatial-frequency velocity variations, all of which can lead to intricate outcomes (Taborda et al.,
625 2012). Consequently, for applications like enhancing microzonation maps, it's imperative to
626 merge this analysis with elements accounting for HF variability.

627 In conclusion, rapid urban expansion in areas of poor historical instrumentation leaves
628 significant gaps in data for seismic hazard assessment. Furthermore, current methods both

629 require decade long deployment of dense seismic networks in the area of near-future urban
630 development and fail to provide high-resolution assessments that identify areas of strong and
631 weak shaking that could underpin high cost-benefit seismic code classification. The potential of
632 physics based simulations has prompted the evaluation of the seismic wave field across areas of
633 near-future development. The results suggest methods to allow the rapid, high-resolution
634 assessment of geological structure that could lead to risk assessment at unprecedented resolution.

635 **Statements and Declarations**

636 **Acknowledgments**

637 John McCloskey is listed as a co-author in recognition of his significant contributions.
638 Unfortunately, he passed away after the manuscript was ready for submission, and we deeply
639 mourn his loss.

640 Authors thank initial discussions and simulations obtained with the prompt support and guidance
641 from Karim Tarbali, former PDRA at the University of Edinburgh. We thank Gemma Cremen,
642 Chris J. Bean, Mark Naylor, Ian Main, Karen Lythgoe and two anonymous reviewers for
643 providing constructive feedback and guidance in improving the manuscript.

644 **Funding**

645 This research is a part of the wider PhD project ‘Physics-based Ground Motion Simulations and
646 Uncertainty Assessment in Rapidly Urbanising Environments’. The PhD student is funded by
647 University of Edinburgh, School of Geosciences. This research project is also supported by the
648 Tomorrow Cities Hub (UKRI/GCRF fund under grant NE/S009000/1).

649 **Author Contributions**

650 Both authors contributed to the study conception and design. Material preparation and data
651 analysis were performed by HA. The first draft of the manuscript was prepared by HA including
652 all the figures and text. The text was further reviewed and improved with the help of JM.

653 **Rights Retention Statement**

654 For the purpose of open access, the author has applied a Creative Commons Attribution (CC BY)
655 licence to any Author Accepted Manuscript version arising from this submission.

656 **Open Research**

657 The data used in this research are mainly the simulation outputs, which are extensive in scale.
658 The critical information regarding the crustal domain, earthquake hypocenter, and PGA data,
659 which is pivotal for generating the majority of the manuscript's results, can be found in the
660 supplementary material. For more detailed information on earthquake moment distribution, we
661 encourage readers to refer to Jenkins et al. 2023. The software used to run the simulation is an
662 open-source package, SPEED (Mazzieri et al., 2013). The data analysis and processing is done
663 using Python and the code is available at <https://github.com/himansh78/GroundMotionCalc.git>.

664 **Competing Interests**

665 The authors declare they have no conflict of interest.

666 **References**

- 667 Abrahamson, N. A., Silva, W. J., & Kamai, R. (2014). Summary of the ASK14 ground motion
668 relation for active crustal regions. *Earthquake Spectra*, 30(3), 1025–1055.
669 <https://doi.org/10.1193/070913EQS198M>
- 670 Aki, K. (1993). Local site effects on weak and strong ground motion. *Tectonophysics*, 218(1–3),
671 93–111. [https://doi.org/10.1016/0040-1951\(93\)90262-I](https://doi.org/10.1016/0040-1951(93)90262-I)
- 672 Ancheta, T. D., Darragh, R. B., Stewart, J. P., Seyhan, E., Silva, W. J., Chiou, B. S. J., ...
673 Donahue, J. L. (2014). NGA-West2 database. *Earthquake Spectra*, 30(3), 989–1005.
674 <https://doi.org/10.1193/070913EQS197M>
- 675 Anderson, J. G., & Brune, J. N. (1999). Probabilistic Seismic Hazard Analysis without the
676 Ergodic Assumption. *Seismological Research Letters*, 70(1), 19–28.
677 <https://doi.org/10.1785/GSSRL.70.1.19>
- 678 Ansal, A., Kurtuluş, A., & Tönük, G. (2010). Seismic microzonation and earthquake damage

679 scenarios for urban areas. *Soil Dynamics and Earthquake Engineering*, 30(11), 1319–1328.
680 <https://doi.org/10.1016/j.soildyn.2010.06.004>

681 Asimaki, D., Ledezma, C., Montalva, G. A., Tassara, A., Mylonakis, G., & Boroschek, R.
682 (2012). Site effects and damage patterns. *Earthquake Spectra*, 28(S1), S55–S74.
683 <https://doi.org/10.1193/1.4000029>

684 Asimaki, D., Mohammadi, K., Mason, H. B., Adams, R. K., Rajaure, S., & Khadka, D. (2017).
685 Observations and Simulations of Basin Effects in the Kathmandu Valley during the 2015
686 Gorkha, Nepal, Earthquake Sequence: *Earthquake Spectra*, 33(S1), S35–S53.
687 <https://doi.org/10.1193/013117EQS022M>

688 Atkinson, G. M., & Boore, D. M. (2006). Earthquake Ground-Motion Prediction Equations for
689 Eastern North America. *Bulletin of the Seismological Society of America*, 96(6), 2181–
690 2205. <https://doi.org/10.1785/0120050245>

691 Baker, J. W., Bradley, B. A., & Stafford, P. J. (2021). *Probabilistic seismic hazard and risk*
692 *analysis*. Cambridge University Press.

693 Bazzurro, P., & Cornell, C. A. (2004). Nonlinear soil-site effects in probabilistic seismic-hazard
694 analysis. *Bulletin of the Seismological Society of America*, 94(6), 2110–2123.
695 <https://doi.org/10.1785/0120030216>

696 Bielak, J., Xu, J., & Ghattas, O. (1999). Earthquake Ground Motion and Structural Response in
697 Alluvial Valleys. *Journal of Geotechnical and Geoenvironmental Engineering*, 125(5),
698 413–423. [https://doi.org/https://doi.org/10.1061/\(ASCE\)1090-0241\(1999\)125:5\(413\)](https://doi.org/https://doi.org/10.1061/(ASCE)1090-0241(1999)125:5(413))

699 Borchardt, R. D., & Glassmoyer, G. (1992). On the characteristics of local geology and their
700 influence on ground motions generated by the Loma Prieta earthquake in the San Francisco
701 Bay region, California. *Bulletin of the Seismological Society of America*, 82(2), 603–641.
702 <https://doi.org/10.1785/BSSA0820020603>

703 Bradley, B. A. (2011). A framework for validation of seismic response analyses using
704 seismometer array recordings. *Soil Dynamics and Earthquake Engineering*, 31(3), 512–520.
705 <https://doi.org/10.1016/j.soildyn.2010.11.008>

- 706 Bradley, B. A. (2015). Systematic ground motion observations in the Canterbury earthquakes
707 and region-specific non-ergodic empirical ground motion modeling. *Earthquake Spectra*,
708 *31*(3), 1735–1761. [https://doi.org/https://doi.org/10.1193/053013EQS137M](https://doi.org/10.1193/053013EQS137M)
- 709 Bradley, B. A. (2019). On-going challenges in physics-based ground motion prediction and
710 insights from the 2010–2011 Canterbury and 2016 Kaikoura, New Zealand earthquakes.
711 *Soil Dynamics and Earthquake Engineering*, *124*, 354–364.
712 <https://doi.org/10.1016/j.soildyn.2018.04.042>
- 713 Brocher, T. M. (2005). Empirical Relations between Elastic Wavespeeds and Density in the
714 Earth’s Crust. *Bulletin of the Seismological Society of America*, *95*(6), 2081–2092.
715 <https://doi.org/10.1785/0120050077>
- 716 Brocher, T. M. (2008). Compressional and shear-wave velocity versus depth relations for
717 common rock types in northern California. *Bulletin of the Seismological Society of America*,
718 *98*(2), 950–968. <https://doi.org/10.1785/0120060403>
- 719 Cadet, H., Macau, A., Benjumea, B., Bellmund, F., & Figueras, S. (2011). From ambient noise
720 recordings to site effect assessment: The case study of Barcelona microzonation. *Soil*
721 *Dynamics and Earthquake Engineering*, *31*(3), 271–281.
722 <https://doi.org/10.1016/J.SOILDYN.2010.07.005>
- 723 Campbell, K. W., & Bozorgnia, Y. (2014). NGA-West2 ground motion model for the average
724 horizontal components of PGA, PGV, and 5% damped linear acceleration response spectra.
725 *Earthquake Spectra*, *30*(3), 1087–1114. <https://doi.org/10.1193/062913EQS175M>
- 726 Castellaro, S., Mulargia, F., & Rossi, P. L. (2008). Vs30: Proxy for seismic amplification?
727 *Seismological Research Letters*, *79*(4), 540–543. <https://doi.org/10.1785/gssrl.79.4.540>
- 728 Castellaro, S., & Musinu, G. (2023). Resonance versus Shape of Sedimentary Basins. *Bulletin of*
729 *the Seismological Society of America*, *113*(2), 745–761. <https://doi.org/10.1785/0120210277>
- 730 Chiou, B. S. J., & Youngs, R. R. (2014). Update of the Chiou and Youngs NGA model for the
731 average horizontal component of peak ground motion and response spectra. *Earthquake*
732 *Spectra*, *30*(3), 1117–1153. <https://doi.org/10.1193/072813EQS219M>

- 733 Cramer, C. H. (2003). Site-specific seismic-hazard analysis that is completely probabilistic.
734 *Bulletin of the Seismological Society of America*, 93(4), 1841–1846.
735 <https://doi.org/10.1785/0120020206>
- 736 Cremen, G., Galasso, C., McCloskey, J., Barcena, A., Creed, M., Filippi, M. E., ... Trogrlić, R.
737 Š. (2023). A state-of-the-art decision-support environment for risk-sensitive and pro-poor
738 urban planning and design in Tomorrow's cities. *International Journal of Disaster Risk*
739 *Reduction*, 85, 103400. <https://doi.org/10.1016/j.ijdr.2022.103400>
- 740 Day, S. M., Graves, R., Bielak, J., Dreger, D., Larsen, S., Olsen, K. B., ... Ramirez-Guzman, L.
741 (2019). Model for Basin Effects on Long-Period Response Spectra in Southern California:
742 *Earthquake Spectra*, 24(1), 257–277. <https://doi.org/10.1193/1.2857545>
- 743 De Hoop, A. T. (1958). Representation theorems for the displacement in an elastic solid and their
744 application to elastodynamic diffraction theory . In *Technische Hogeschool, Delft,*
745 *Netherland*. Technische Hogeschoo.
- 746 Dolce, M., Masi, A., Marino, M., & Vona, M. (2003). Earthquake damage scenarios of the
747 building stock of Potenza (Southern Italy) including site effects. *Bulletin of Earthquake*
748 *Engineering*, 1(1), 115–140. <https://doi.org/10.1023/A:1024809511362>
- 749 Douglas, J. (2017). Ground motion prediction equations 1964-2019 (December 2019). *SED*
750 *Report SED/ENSI/R/01/20140911, October*, 1–651.
751 <http://www.gmpe.org.uk/gmpereport2014.pdf>
- 752 Douglas, J., & Aochi, H. (2008). A survey of techniques for predicting earthquake ground
753 motions for engineering purposes. *Surveys in Geophysics*, 29(3), 187–220.
754 <https://doi.org/10.1007/s10712-008-9046-y>
- 755 Douglas, J., & Edwards, B. (2016a). Recent and future developments in earthquake ground
756 motion estimation. *Earth-Science Reviews*, 160, 203–219.
757 <https://doi.org/10.1016/j.earscirev.2016.07.005>
- 758 Douglas, J., & Edwards, B. (2016b). Recent and future developments in earthquake ground
759 motion estimation. In *Earth-Science Reviews* (Vol. 160, pp. 203–219). Elsevier B.V.

760 <https://doi.org/10.1016/j.earscirev.2016.07.005>

761 Foti, S., Aimar, M., Ciancimino, A., & Passeri, F. (2019). Recent developments in seismic site
762 response evaluation and microzonation. *Proceedings of the 17th European Conference on*
763 *Soil Mechanics and Geotechnical Engineering, ECSMGE 2019*.
764 <https://doi.org/10.32075/17ECSMGE-2019-1117>

765 Frankel, A. (1993). Three-dimensional simulations of ground motions in the San Bernardino
766 Valley, California, for hypothetical earthquakes on the San Andreas Fault. *Bulletin of*
767 *Seismological Society of America*, 83(4), 1020–1041.
768 <https://doi.org/https://doi.org/10.1785/BSSA0830041020>

769 Freddi, F., Galasso, C., Cremen, G., Dall’Asta, A., Di Sarno, L., Giaralis, A., ... Woo, G. (2021).
770 Innovations in earthquake risk reduction for resilience: Recent advances and challenges.
771 *International Journal of Disaster Risk Reduction*, 60.
772 <https://doi.org/10.1016/j.ijdr.2021.102267>

773 García-Pérez, T., Ferreira, A. M. G., Yáñez, G., Iturrieta, P., & Cembrano, J. (2021). Effects of
774 topography and basins on seismic wave amplification: The Northern Chile coastal cliff and
775 intramountainous basins. *Geophysical Journal International*, 227(2), 1143–1167.
776 <https://doi.org/10.1093/gji/ggab259>

777 Geli, L., Bard, P. Y., & Jullien, B. (1988). The effect of topography on earthquake ground
778 motion: a review and new results. In *Bulletin - Seismological Society of America* (Vol. 78,
779 Issue 1, pp. 42–63). [https://doi.org/10.1016/0148-9062\(88\)90024-1](https://doi.org/10.1016/0148-9062(88)90024-1)

780 Gentile, R., Cremen, G., Galasso, C., Jenkins, L. T., Manandhar, V., Mentese, E. Y., ...
781 McCloskey, J. (2022). Scoring , selecting , and developing physical impact models for
782 multi- hazard risk assessment. *International Journal of Disaster Risk Reduction*, 82,
783 103365. <https://doi.org/https://doi.org/10.1016/j.ijdr.2022.103365>

784 Graves, R. W., & Pitarka, A. (2010). Broadband ground-motion simulation using a hybrid
785 approach. *Bulletin of the Seismological Society of America*, 100(5 A), 2095–2123.
786 <https://doi.org/10.1785/0120100057>

- 787 Graves, R. W., Pitarka, A., & Somerville, P. G. (1998). Ground-motion amplification in the
788 Santa Monica area: Effects of shallow basin-edge structure. *Bulletin of the Seismological*
789 *Society of America*, 88(5), 1224–1242. <https://doi.org/10.1785/bssa0880051224>
- 790 Hough, S. E., & Anderson, J. G. (1988). High-frequency Spectra Observed at Anza, California:
791 Implications for Q Structure. *Bulletin of the Seismological Society of America*, 78(2), 692–
792 707. <https://doi.org/https://doi.org/10.1785/BSSA0780020692>
- 793 Hough, S. E., Martin, S. S., Gahalaut, V., Joshi, A., Landes, M., & Bossu, R. (2016). A
794 comparison of observed and predicted ground motions from the 2015 MW7.8 Gorkha,
795 Nepal, earthquake. *Natural Hazards*, 84(3), 1661–1684.
796 <https://doi.org/https://doi.org/10.1007/s11069-016-2505-8>
- 797 Jenkins, L. T., Creed, M. J., Tarbali, K., Muthusamy, M., Trogrlić, R. Š., Phillips, J. C., ...
798 McCloskey, J. (2023). Physics-based simulations of multiple natural hazards for risk-
799 sensitive planning and decision-making in expanding urban regions. *International Journal*
800 *of Disaster Risk Reduction*, 84, 103338.
801 <https://doi.org/https://doi.org/10.1016/j.ijdr.2022.103338>
- 802 Kaklamanos, J., Bradley, B. A., Thompson, E. M., & Baise, L. G. (2013). Critical parameters
803 affecting bias and variability in site-response analyses using KiK-net downhole array data.
804 *Bulletin of the Seismological Society of America*, 103(3), 1733–1749.
805 <https://doi.org/10.1785/0120120166>
- 806 Kamai, R., Abrahamson, N. A., & Silva, W. J. (2016). VS30 in the NGA GMPEs: Regional
807 differences and suggested practice. *Earthquake Spectra*, 32(4), 2083–2108.
808 <https://doi.org/10.1193/072615EQS121M>
- 809 Kiureghian, A. Der, & Ditlevsen, O. (2009). Aleatory or epistemic? Does it matter? *Structural*
810 *Safety*, 31(2), 105–112. <https://doi.org/10.1016/j.strusafe.2008.06.020>
- 811 Knopoff, L. (1956). Diffraction of Elastic Waves. *The Journal of the Acoustical Society of*
812 *America*, 28, 217. <https://doi.org/10.1121/1.1908247>
- 813 Kramer, S. L. (1996). *Geotechnical Earthquake Engineering*. Pearson Prentice-Hall, Upper

814 Saddle River, NJ, USA.

815 Kramer, S. L., & Mitchell, R. A. (2006). Ground Motion Intensity Measures for Liquefaction
816 Hazard Evaluation: *Earthquake Spectra*, 22(2), 413–438. <https://doi.org/10.1193/1.2194970>

817 Kuehn, N. M., Abrahamson, N. A., & Walling, M. A. (2019). Incorporating Nonergodic Path
818 Effects into the NGA-West2 Ground-Motion Prediction Equations. *Bulletin of the*
819 *Seismological Society of America Seismological Society of America*, 109(2), 575–585.
820 <https://doi.org/10.1785/0120180260>

821 Landwehr, N., Kuehn, N. M., Scheffer, T., & Abrahamson, N. (2016). A Nonergodic Ground-
822 Motion Model for California with Spatially Varying Coefficients. *Bulletin of the*
823 *Seismological Society of America*, 6, 2574–2583. <https://doi.org/10.1785/0120160118>

824 Lee, S. J., Komatitsch, D., Huang, B. S., & Tromp, J. (2009). Effects of topography on seismic-
825 wave propagation: An example from Northern Taiwan. *Bulletin of the Seismological Society*
826 *of America*, 99(1), 314–325. <https://doi.org/10.1785/0120080020>

827 Liu, P., Archuleta, R. J., & Hartzell, S. H. (2006). *Prediction of Broadband Ground-Motion Time*
828 *Histories : Hybrid Low / High- Frequency Method with Correlated Random Source*
829 *Parameters*. 96(6), 2118–2130. <https://doi.org/10.1785/0120060036>

830 Marafi, N. A., Eberhard, M. O., Berman, J. W., Wirth, E. A., & Frankel, A. D. (2017). Effects of
831 deep basins on structural collapse during large subduction earthquakes. *Earthquake Spectra*,
832 33(3), 963–997. <https://doi.org/10.1193/071916EQS114M>

833 Maufroy, E., Cruz-Atienza, V. M., & Gaffet, S. (2012). A robust method for assessing 3-D
834 topographic site effects: A case study at the LSBB underground laboratory, France.
835 *Earthquake Spectra*, 28(3), 1097–1115. <https://doi.org/10.1193/1.4000050>

836 Mazzieri, I., Stupazzini, M., Guidotti, R., & Smerzini, C. (2013). SPEED: SPectral Elements in
837 Elastodynamics with Discontinuous Galerkin: a non-conforming approach for 3D multi-
838 scale problems. *International Journal for Numerical Methods in Engineering*, 95(12), 991–
839 1010. <https://doi.org/10.1002/NME.4532>

- 840 Mazzieri, I., Stupazzini, M., Guidotti, R., Smerzini, C., Mazzieri, I., Stupazzini, M., ... Smerzini,
841 C. (2013). SPEED: SPectral Elements in Elastodynamics with Discontinuous Galerkin: a
842 non-conforming approach for 3D multi-scale problems. *IJNME*, 95(12), 991–1010.
843 <https://doi.org/10.1002/NME.4532>
- 844 Mcguire, R. K. (2008). Probabilistic seismic hazard analysis: Early history. *Earthquake*
845 *Engineering & Structural Dynamics*, 37, 329–338. <https://doi.org/10.1002/eqe.765>
- 846 Menteşe, E. Y., Cremen, G., Gentile, R., Galasso, C., Filippi, E. M., & McCloskey, J. (2023).
847 Future exposure modelling for risk-informed decision making in urban planning.
848 *International Journal of Disaster Risk Reduction*, 90, 103651.
849 <https://doi.org/10.1016/j.ijdr.2023.103651>
- 850 Mucciarelli, M., & Gallipoli, M. R. (2006). Comparison between Vs30 and other estimates of
851 site amplification in Italy. *First European Conference on Earthquake Engineering and*
852 *Seismology, September*, 270.
- 853 Nath, S. K., & Thingbaijam, K. K. S. (2011). Peak ground motion predictions in India: an
854 appraisal for rock sites. *Journal of Seismology*, 15(2), 295–315.
855 <https://doi.org/https://doi.org/10.1007/s10950-010-9224-5>
- 856 Ohsumi, T., Mukai, Y., & Fujitani, H. (2016). Investigation of Damage in and Around
857 Kathmandu Valley Related to the 2015 Gorkha, Nepal Earthquake and Beyond.
858 *Geotechnical and Geological Engineering*, 34(4), 1223–1245.
859 <https://doi.org/10.1007/s10706-016-0023-9>
- 860 Oral, E., Ayoubi, P., Ampuero, J. P., Asimaki, D., & Bonilla, L. F. (2022). Kathmandu Basin as
861 a local modulator of seismic waves: 2-D modelling of non-linear site response under
862 obliquely incident waves. *Geophysical Journal International*, 231(3), 1996–2008.
863 <https://doi.org/10.1093/gji/ggac302>
- 864 Paolucci, R., Mazzieri, I., Smerzini, C., & Stupazzini, M. (2014). Physics-Based Earthquake
865 Ground Shaking Scenarios in Large Urban Areas. *Geotechnical, Geological and*
866 *Earthquake Engineering*, 34, 331–359. https://doi.org/10.1007/978-3-319-07118-3_10

- 867 Pilz, M., Parolai, S., Stupazzini, M., Paolucci, R., & Zschau, J. (2011). Modelling basin effects
868 on earthquake ground motion in the Santiago de Chile basin by a spectral element code.
869 *Geophys. J. Int*, 187, 929–945. <https://doi.org/10.1111/j.1365-246X.2011.05183.x>
- 870 Pitilakis, K., Riga, E., Anastasiadis, A., Fotopoulou, S., & Karafagka, S. (2019). Towards the
871 revision of EC8: Proposal for an alternative site classification scheme and associated
872 intensity dependent spectral amplification factors. *Soil Dynamics and Earthquake*
873 *Engineering*, 126, 105137. <https://doi.org/10.1016/j.soildyn.2018.03.030>
- 874 Poursartip, B., Fathi, A., & Tassoulas, J. L. (2020). Large-scale simulation of seismic wave
875 motion: A review. *Soil Dynamics and Earthquake Engineering*, 129, 105909.
876 <https://doi.org/10.1016/j.soildyn.2019.105909>
- 877 Rodriguez-Marek, A., Rathje, E. M., Bommer, J. J., Scherbaum, F., & Stafford, P. J. (2014).
878 Application of Single-Station Sigma and Site-Response Characterization in a Probabilistic
879 Seismic-Hazard Analysis for a New Nuclear Site. *Bulletin of Seismological Society of*
880 *America*, 104(4), 1601–1619. <https://doi.org/10.1785/0120130196>
- 881 Schmedes, J., Archuleta, R. J., & Lavalée, D. (2013). A kinematic rupture model generator
882 incorporating spatial interdependency of earthquake source parameters. *Geophysical*
883 *Journal International*, 192(3), 1116–1131. <https://doi.org/10.1093/gji/ggs021>
- 884 Sebastiano, D., Francesco, P., Salvatore, M., Roberto, I., Antonella, P., Giuseppe, L., ... Daniela,
885 F. (2019). Ambient noise techniques to study near-surface in particular geological
886 conditions: A brief review. In *Innovation in Near-Surface Geophysics: Instrumentation,*
887 *Application, and Data Processing Methods* (pp. 419–460). Elsevier Inc.
888 <https://doi.org/10.1016/B978-0-12-812429-1.00012-X>
- 889 Semblat, J. F., Kham, M., Parara, E., Bard, P. Y., Pitilakis, K., Makra, K., & Raptakis, D. (2005).
890 Seismic wave amplification: Basin geometry vs soil layering. *Soil Dynamics and*
891 *Earthquake Engineering*, 25(7–10), 529–538. <https://doi.org/10.1016/j.soildyn.2004.11.003>
- 892 Sextos, A., De Risi, R., Pagliaroli, A., Foti, S., Passeri, F., Ausilio, E., ... Zimmaro, P. (2018).
893 Local site effects and incremental damage of buildings during the 2016 Central Italy

- 894 Earthquake sequence. *Earthquake Spectra*, 34(4), 1639–1669.
895 <https://doi.org/10.1193/100317EQS194M>
- 896 Shi, J., & Asimaki, D. (2017). From Stiffness to Strength: Formulation and Validation of a
897 Hybrid Hyperbolic Nonlinear Soil Model for Site-Response Analyses. *Bulletin of the*
898 *Seismological Society of America*, 107(3), 1336–1355. <https://doi.org/10.1785/0120150287>
- 899 Smerzini, C., Paolucci, R., & Stupazzini, M. (2011). Comparison of 3D, 2D and 1D numerical
900 approaches to predict long period earthquake ground motion in the Gubbio plain, Central
901 Italy. *Bulletin of Earthquake Engineering*, 9(6), 2007–2029. [https://doi.org/10.1007/s10518-](https://doi.org/10.1007/s10518-011-9289-8)
902 011-9289-8
- 903 Smerzini, C., & Villani, M. (2012). Broadband numerical simulations in complex near-field
904 geological configurations: The case of the 2009 Mw 6.3 L'Aquila earthquake. *Bulletin of*
905 *the Seismological Society of America*, 102(6), 2436–2451.
906 <https://doi.org/10.1785/0120120002>
- 907 Spudich, P., Bayless, J. R., Baker, J., Chiou, B. S. J., Rowshandel, B., Shahi, S., & Somerville,
908 P. (2013). Final Report of the NGA-West2 Directivity Working Group. In *Pacific*
909 *Engineering Research Center Report* (Issue 09).
- 910 Stewart, J. P., Afshari, K., & Goulet, C. A. (2017). Non-ergodic site response in seismic hazard
911 analysis. *Earthquake Spectra*, 33(4), 1385–1414. <https://doi.org/10.1193/081716EQS135M>
- 912 Stirling, M. W. (2014). The Continued Utility of Probabilistic Seismic-Hazard Assessment. In
913 *Earthquake Hazard, Risk and Disasters* (pp. 359–376). Elsevier Inc.
914 <https://doi.org/10.1016/B978-0-12-394848-9.00013-4>
- 915 Stirling, M. W., McVerry, G., Gerstenberger, M., Litchfield, N., Van Dissen, R., Berryman, K.,
916 ... Jacobs, K. (2012). National seismic hazard model for New Zealand: 2010 update.
917 *Bulletin of the Seismological Society of America*, 102(4), 1514–1542.
918 <https://doi.org/10.1785/0120110170>
- 919 Taborda, R., Bielak, J., & Restrepo, D. (2012). Earthquake Ground-Motion Simulation including
920 Nonlinear Soil Effects under Idealized Conditions with Application to Two Case Studies.

- 921 *Seismological Research Letters*, 83(6), 1047–1060. <https://doi.org/10.1785/0220120079>
- 922 Taborda, R., Roten, D., & Diego, S. (2014). Physics-Based Ground-Motion Simulation. In
923 *Encyclopedia of Earthquake Engineering* (Issue January, pp. 1–33).
924 <https://doi.org/10.1007/978-3-642-36197-5>
- 925 Torre, C. A. de la, Bradley, B. A., & Lee, R. L. (2020). Modeling nonlinear site effects in
926 physics-based ground motion simulations of the 2010–2011 Canterbury earthquake
927 sequence: *Earthquake Spectra*, 36(2), 856–879. <https://doi.org/10.1177/8755293019891729>
- 928 Tsai, C. C., Kishida, T., & Lin, W. C. (2021). Adjustment of site factors for basin effects from
929 site response analysis and deep downhole array measurements in Taipei. *Engineering*
930 *Geology*, 285(June 2020), 106071. <https://doi.org/10.1016/j.enggeo.2021.106071>
- 931 UN-Habitat. (2022). World Cities Report 2020: Envisaging the Future of Cities. In *World Cities*
932 *Report 2020: Envisaging the Future of Cities*. UN.
- 933 UNISDR, U. (2015). Sendai framework for disaster risk reduction 2015-2030. *Proceedings of*
934 *the 3rd United Nations World Conference on DRR*.
- 935 Wang, C., Cremen, G., Gentile, R., & Galasso, C. (2023). Design and assessment of pro-poor
936 financial soft policies for expanding cities. *International Journal of Disaster Risk*
937 *Reduction*, 85(December 2022), 103500. <https://doi.org/10.1016/j.ijdr.2022.103500>
- 938 Wang, G., Du, C., Huang, D., Jin, F., Koo, R. C. H., & Kwan, J. S. H. (2018). Parametric models
939 for 3D topographic amplification of ground motions considering subsurface soils. *Soil*
940 *Dynamics and Earthquake Engineering*, 115(September 2017), 41–54.
941 <https://doi.org/10.1016/j.soildyn.2018.07.018>
- 942 Wells, D. L., & Coppersmith, K. J. (1994). New empirical relationships among magnitude,
943 rupture length, rupture width, rupture area, and surface displacement. *Bulletin -*
944 *Seismological Society of America*, 84(4), 974–1002.
945 <https://doi.org/10.1785/bssa0840040974>
- 946 Yomogida, K., & Etgen, J. T. (1993). 3-D wave propagation in the Los Angeles Basin for the

947 Whittier-Narrows earthquake. *Bulletin of the Seismological Society of America*, 83(5),
948 1325–1344. <https://doi.org/10.1086/622062>

949 Zhu, C., Thambiratnam, D., & Gallage, C. (2018). Statistical analysis of the additional
950 amplification in deep basins relative to the 1D approach. *Soil Dynamics and Earthquake*
951 *Engineering*, 104, 296–306. <https://doi.org/10.1016/j.soildyn.2017.09.003>

952